Catalysis Today 438 (2024) 114788

Contents lists available at ScienceDirect

Catalysis Today

journal homepage: www.elsevier.com/locate/cattod

Strategies to improve CO tolerance and corrosion resistance of Pt electrocatalysts for polymer electrolyte membrane fuel cells: Sn-doping of the mixed oxide–carbon composite support

Irina Borbáth [a,*], Khirdakhanim Salmanzade [a], Zoltán Pászti [a], Andrei Kuncser [b], Dana Radu [b], Ştefan Neaţu [b], Emília Tálas [a], István E. Sajó [c], Dániel Olasz [d], György Sáfrán [d], Ágnes Szegedi [a], Mihaela Florea [b], András Tompos [a]

[a] HUN-REN Research Centre for Natural Sciences, Institute of Materials and Environmental Chemistry, Magyar Tudósok körútja 2, Budapest H-1117, Hungary
[b] National Institute of Materials Physics, 405A Atomistilor Street, Magurele 077125, Romania
[c] University of Pécs, Szentágothai Research Centre, Ifjúság u. 20, Pécs H-7624, Hungary
[d] HUN-REN Centre for Energy Research, Institute for Technical Physics and Materials Science, Konkoly-Thege Miklós út 29-33, Budapest H-1121, Hungary

ARTICLE INFO

Keywords:
Anode Pt electrocatalysts
$TiSnO_x$
Ti-based mixed oxide–carbon composite
CO-tolerance
Sn-Pt interactions

ABSTRACT

Design of composite support materials based on Sn-doped TiO_2 and carbon is one of the strategies to develop corrosion-resistant and CO-tolerant Pt electrocatalysts for polymer electrolyte membrane (PEM) fuel cells. As the synthesis methodology may have crucial influence on the structural and functional properties of the composites, different preparation routes for the novel support materials are explored and compared. $Ti_{(1-x)}Sn_xO_2$–C (x: 0.1–0.3) composites with different mixed oxide/carbon ratios were prepared by two sol-gel-based synthesis routes, namely (i) the introduction of a Sn precursor after the formation of the TiO_2-rutile nuclei on the carbon backbone (route ***A***), and (ii) simultaneous introduction of Ti and Sn precursors, resulting in good mixing of the Sn- and Ti-sol before the addition of the carbon (route ***B***). The bulk and surface microstructure of the composites and the electrocatalysts obtained by their Pt-loading were investigated in detail. The incorporation of tin into the TiO_2-rutile unit cell was confirmed by X-ray powder diffraction and Raman spectroscopy; the results indicated doping levels in good accordance with the amount of tin precursor. The advantages of composites and Pt electrocatalysts obtained via synthesis route ***B*** were that they do not contain segregated Sn^0 or SnO_2 phases, have a more homogeneous/uniform mixed oxide distribution over the carbon backbone, and the electrochemically active surface area values (~60–80 m^2/g_{Pt}) are twice as high as those of catalysts with similar compositions synthesized by method ***A***. A common feature of the composites prepared by routes ***A*** and ***B*** was the presence of a tin oxide-rich overlayer identified by X-ray photoelectron spectroscopy. As a consequence, the electrocatalytic behavior of the catalysts was not influenced by the Ti/Sn ratio and was mainly dependent on the synthesis method used in the preparation of composite support materials. Elemental maps confirmed the formation of areas where Pt and the Sn doping element were in atomic proximity to each other, which means a favorable interaction either for the bifunctional mechanism or the electronic ligand effect. An increase in carbon content in composite materials led to an increase in both catalytic activity and long-term stability. The results of electrochemical studies showed that Sn-containing Pt catalysts with a high carbon content (75 wt%) are the most promising for potential use both as an anode and a cathode for PEM fuel cells.

1. Introduction

Satisfying the energy needs of humanity without the formation of toxic or harmful substances is a particularly important task. Fuel cells are regarded as important alternative energy converters and key technology for future sustainable energy systems. Due to their low operation temperature/pressure requirement and high energy density, Polymer Electrolyte Membrane (PEM) fuel cells comprise the most important type of fuel cells for different applications from automobiles to small-scale electricity generation. The market penetration of PEM fuel

* Correspondence to: P.O.Box 286, (Irina Borbáth), Budapest H-1519, Hungary.
E-mail address: borbath.irina@ttk.hu (I. Borbáth).

https://doi.org/10.1016/j.cattod.2024.114788
Received 30 January 2024; Received in revised form 26 April 2024; Accepted 3 May 2024
Available online 9 May 2024

cells is mainly prevented by their high cost. The most expensive component of these cells is the electrocatalyst, which accounts for about one-third of the total cost [1]. Currently, Pt supported on high surface area carbon (Pt/C) is still the most widely used state-of-the-art catalyst in PEM fuel cells, although it is prone to electrocorrosion under steady operating conditions of the cells (0.6–0.9 V), start-up shutdown period, fuel starvation or polarity reversal, all of which lead to loss of activity [2,3]. This problem, along with the limited efficiency of the Pt/C catalyst in the oxygen reduction reaction (ORR), is usually compensated by high Pt loadings, especially at the cathode electrode.

In order to facilitate widespread use of PEM fuel cells, development of more affordable systems is needed, which involves replacement of the traditional Pt/C electrocatalysts with more corrosion resistant and cheaper ones [4]. Therefore, the key challenge is to develop (i) highly active and durable Pt and Pt-based catalysts and (ii) highly stable catalyst support materials with adequate electrical conductivity, excellent corrosion resistance and superior proton transport properties [5].

Another problem that has to be taken into account with the Pt/C electrocatalysts is their sensitivity to CO poisoning, which makes hydrogen fuel from steam reforming unsuitable for PEM cells without further purification [6]. A common approach to solving the problem of CO-related catalyst poisoning is to use a oxophilic surface metal with co-catalytic properties located in atomic proximity to the Pt [7]. In general, reactive hydroxyl groups are more easily formed on the oxophilic dopant than on Pt, which not only facilitates the easy oxidation of the CO impurity through the so-called bifunctional mechanism at the anode [8–10], but is also beneficial in the much slower process at the cathode electrode [11,12]. Among the strategies using oxophilic additives to improve the CO tolerance of anode Pt electrocatalysts, the most common are (i) the development of binary and ternary Pt alloys, (ii) the use of Pt-based electrocatalysts in combination with metal oxides, (iii) and the replacement of carbon supports with transition metal oxides [13,14].

Despite the fact that reducible oxophilic metal oxides are valuable co-catalysts or supports for PEM fuel cell electrocatalysts, their dissolution under cell operating conditions is still a serious problem, since dissolved metal cations can be absorbed by the polymer membrane, resulting in the loss of its ability to conduct protons [15]. In addition to this, the crossover of dissolved metal cations through the membrane with subsequent deposition on the cathode Pt catalyst suppresses the ORR rate due to blocking of Pt sites, which leads to rapid oxidation and deactivation of the cathode catalyst [16,17].

The serious leaching problems may be avoided by using the oxide of the oxophilic component as support or support modifier if it is stable in the expected potential window. In general, metal oxides exhibit better thermodynamic stability and higher corrosion resistance in acidic environments than their corresponding metallic forms. Considering this, it would be desirable to use more stable metal oxide-based support to improve the stability of the catalyst.

Numerous studies have been conducted to develop metal oxides (e.g., TiO_2 [18–20], WO_3/WO_x [21–25], MoO_x [26,27] and SnO_2 [28,29]) with high corrosion resistance as potential support materials for electrocatalysts [30], which can also act as co-catalysts for enhancing catalytic activity. It is necessary to emphasize that in the literature on this topic, special attention is paid to increasing the stability of metal oxides in acidic environments using effective approaches (e.g., the creation of oxides with special structures and heterostructures) [31].

Among the transition metal oxides, titania and tin oxide have primarily attracted extensive attention of researchers as promising support materials for fuel cell applications, since they are assumed to be chemically inert and stable even under harsh cathodic conditions [32]. In ref. [33], based on studies of Pt electrocatalysts supported on MoO_3, SnO_2, Nb_2O_5, Ta_2O_5, TiO_2, and WO_3 oxides, performed using experimental protocols simulating realistic fuel cell operation conditions, it was concluded that Pt/SnO_2 has superior performance in terms of electrochemical activity and dissolution resistance.

Unfortunately, it should be noted that the generally rather low electrical conductivity of metal oxides is a serious problem for their widespread use as a support for electrocatalysts. The simplest and most frequently used method for increasing the conductivity of oxide-based supported catalysts is both their mixing with carbon powder [34] and the preparation of carbon-containing oxide-based composite support materials (e.g., SnO_2-based [35–43] and TiO_2-based [44–47] ones). It is necessary to mention that noble metal-mixed oxide-carbon triple junctions, leading to a strong interaction of the active metal with the composite support, play an important role in increasing the stability and activity of the catalytic systems, which has been confirmed not only experimentally, but also by density functional theory (DFT) calculations [48]. For example, it has been demonstrated [49] that a promising composite support material based on electrically conductive carbon nanofibers (CFs) decorated with non-conductive stabilizing SnO_2 provides high catalyst stability to the SnO_2/Pt/CFs electrocatalyst.

According to the literature [50], in the field of electrocatalysis the most attractive novel oxide-type support materials include sub-stoichiometric metal oxides (e.g., Ti_4O_7 and Ebonex), nanostructured metal oxides (e.g., nanowires [51] and nanofibers of SnO_2 [52,53]) and metal-doped oxides. Among the listed methods for improving electrical conductivity, the most common is the introduction of an appropriate dopant through cationic substitution, assuming that doping does not radically change the chemical stability of the host oxide lattice. Based on metal-doped oxide, a novel class of electrocatalysts including Pt supported on various transition metals (M)-doped TiO_2 (M: W [54], Mo [55,56], Nb [57,58], Ta [59,60], Sn [61], etc.) has been developed for potential use in PEM fuel cells.

It should be noted that the combination of titania and tin oxide in Ti-Sn mixed oxide composite materials can be very interesting from many points of view. Well-established sensing properties of SnO_2 for reductive gases, combined with the good chemical stability of TiO_2 at high temperatures, stimulate the research on the application of TiO_2–SnO_2 solid solutions, for example, in gas detection [62]. In the literature there are numerous variants of methods for obtaining Sn–doped TiO_2 materials by the sol-gel [63–67], co-precipitation [68], solvothermal synthesis method [69], mechanochemical synthesis [70,71], the citric acid complexing method [72], plasma-enhanced chemical vapor deposition [73], template-based liquid phase deposition method [74] and fluoride-mediated chemically induced self-transformation strategy [75]. It is important to note that the successful Sn doping into the TiO_2 lattice with a replacement of the Ti^{4+} position led to a phase transition from anatase to rutile for TiO_2 samples. In turn, this also provides indirect evidence of Sn doping into TiO_2 [76,77].

Several attempts have been made to prepare Pt electrocatalysts supported on supports containing Ti-Sn mixed oxides. Thus, $Ti_{0.7}Sn_{0.3}O_2$ nanoparticles with appropriate surface area of 125.7 $m^2\ g^{-1}$ and electronic conductivity of about 1.07×10^{-4} S cm^{-1}, which is significantly higher than that of the undoped TiO_2 NPs (1.42×10^{-7} S cm^{-1}), were successfully used as the cathode catalyst support in PEM fuel cells [61]. Compared with the Pt/C (C: Vulcan XC-72), the $Pt/Ti_{0.7}Sn_{0.3}O_2$ catalyst shows enhanced stability under both high potential hold (at 1.4 V for 10 h) and potential cycling between 0.6 and 1.2 V vs. NHE.

In ref. [78], Sn/Ti ratios in the $Ti_{1-x}Sn_xO_2$ (x: 0.1–0.3) solid-solution and $Ti_{1-x}Sn_xO_2$/C (C: Vulcan XC-72) ratios in hybrid $Ti_{1-x}Sn_xO_2$–C support materials were systematically optimized in terms of their performance as supports for methanol electrooxidation. The best characteristics were obtained on the 20 wt% $Pt/Ti_{0.9}Sn_{0.1}O_2$–C electrocatalyst, which exhibits higher activity and durability compared to Pt/TiO_2–C and commercial Pt/C.

Our approach is the development of mixed oxide–carbon composite supported Pt electrocatalyst. In our previous studies this concept was implemented by synthesizing anode Pt electrocatalysts supported on a conductive and corrosion resistant composite consisting of oxophilic metal M (M: W, Mo)-doped TiO_2 and various carbonaceous materials [79,80]. In such a unique material system, the corrosion resistance and

nanoparticle-stabilizing ability of TiO_2, the good co-catalytic properties of doping metals as well as the large surface area and high conductivity of active carbon are combined (see Scheme 1). As noted earlier, to overcome the leaching of oxophilic metals in an acidic electrolyte, the ideal solution is the development of composite supports in which the co-catalyst metal can be stabilized by incorporating it into the rutile phase titanium dioxide lattice. The strong interaction between Pt, the TiO_2-rutile phase and the dopant M (M: W, Mo, Nb, and Sn) can be exploited to improve the electrocatalytic properties. The role of transition metal dopant is to facilitate the oxidation of CO at much lower potentials than pure Pt on anode electrode as well as to improve activity in the much slower process at the cathode side.

The most important task of this method is to improve the synthesis of composite support, i.e., the formation of a uniform coating of the carbon backbone with small mixed oxide crystallites (without sintering into large agglomerates) and the complete incorporation of the dopant M, which prevents its dissolution [81]. Indeed, as shown by our results obtained in a three-electrode electrochemical cell [82] and tests carried out in fuel cell [83,84], Pt electrocatalysts supported on W- or Mo-doped rutile – carbon composites were not only resistant to CO poisoning, but also, due to the presence oxide-carbon-Pt triple junctions, showed much better long-term stability compared to the reference Pt/C. However, Sn-based composite support systems have not yet been dealt with in our laboratory.

Thus, our aim is to develop an optimized synthesis route for the preparation of novel $Ti_{(1-x)}Sn_xO_2$–C (x: 0.1–0.3) composite supported Pt electrocatalysts using both our multistep sol-gel synthesis developed for Mo-containing composites, and a new synthesis route based on the simultaneous addition of Ti and Sn precursors, which is hypothesized to lead to the formation of a precursor of Ti–Sn mixed oxides before the addition of carbonaceous material. Using a combination of structural, spectroscopic and electrochemical methods we have analyzed the effect of the Ti/Sn and mixed oxide/carbon ratios in the support on the CO tolerance, activity and stability of Pt electrocatalysts prepared by both preparation routes, to determine the optimal composition for the composite supported catalyst with 20 wt% Pt loading. A comparison of the activity of the best Sn- and Mo-containing Pt catalysts has been carried out in order to study the effect of the type of doping metal M in the $Ti_{(1-x)}M_xO_2$–C composite as a strategy for improving the electrocatalytic performance of these catalytic systems.

2. Materials and methods

2.1. Materials

The $Ti_{(1-x)}Sn_xO_2$–C (x: 0.1–0.3) composite supports were prepared using Black Pearls 2000 (Cabot Corporation, denominated as BP) as the carbonaceous material. Ti and Sn precursor compounds were titanium-isopropoxide (Ti(O-*i*-*Pr*)$_4$, Sigma-Aldrich, 97%) and tin (IV) chloride-5-hydrate ($SnCl_4 \times 5\ H_2O$, Honeywell Riedel-de Haën GmbH, 98%). For the composite synthesis, nitric acid (HNO_3, Molar Chemicals, 65%, a.r.) and ultrapure water (18 MΩ cm, produced by Millipore equipment) were used.

The Pt precursor for electrocatalyst synthesis was hexachloroplatinic acid hexahydrate ($H_2PtCl_6 \times 6\ H_2O$, Sigma-Aldrich, 37.5% Pt). Ethanol (99.55%), HCl (37%), ethylene-glycol (EG, 99.8%) and sodium borohydride ($NaBH_4$, 99.95%) (all obtained from Molar Chemicals) were also used for Pt loading.

The catalyst ink for the electrochemical studies was prepared using a Nafion solution (DuPont™ Nafion® PFSA Polymer Dispersions DE 520), 2-propanol (*i*-C_3H_5OH, Molar Chemicals, 99.9 V/V%, a.r) and ultrapure water (see above). The gases (H_2, N_2, Ar) used in this work were products of Linde Gáz Magyarország Zrt. with 5.0 purity. Reference 20 wt% Pt/C electrocatalyst (C: Vulcan XC-72) was the product of Quintech.

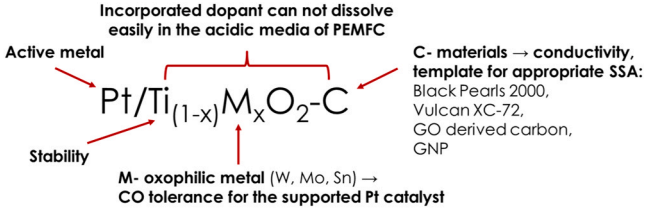

Scheme 1. Our strategy for development of Pt electrocatalysts with improved CO tolerance and corrosion resistance for implementation in PEM fuel cells.

2.2. Preparation of $Ti_{(1-x)}Sn_xO_2$–C (x: 0.1–0.3) composite materials and Pt electrocatalysts

At first, for the synthesis of new type of tin-containing composites, the technique we developed for $Ti_{0.8}Mo_{0.2}O_2$–C materials with mixed oxide/carbon ratio of 75/25 was adapted [82] (route ***A***).

As shown in Fig. 1, in route ***A*** the Sn precursor was introduced after the aging step, the purpose of which was the formation of the TiO_2-rutile phase deposited onto carbon backbone. In comparison to route ***A***, the main difference in the preparation of composite materials via route ***B*** is that the precursor of Sn was introduced immediately after the formation of the transparent Ti-sol, before the addition of the carbon and the aging step (Fig. 1, route ***B***). Table 1 summarizes the quantities of the titanium and tin precursors as well as amount of the carbonaceous material used in the synthesis of support materials.

Our previous studies [82] showed that the incorporation of doping metal M into the TiO_2-rutile lattice occurs during high-temperature treatment (HTT) in Ar. It should be emphasized that in route ***A*** the HTT step, similar to the synthesis procedure developed for Mo-containing composites, was carried out at 600 °C for 8 hours. It should be noted that in synthesis route ***B***, given that Sn doping promotes the conversion of anatase to rutile at lower temperatures compared to that observed for the undoped TiO_2 [85], the final temperature of the HTT step in Ar was reduced to 500 °C. It was confirmed by supporting experiments that the effect of the heat treatment temperature on the surface properties of the supports is relatively low in the 500–600 °C range, thus the change of the temperature does not affect the comparability of the materials.

As shown in Table 1 the samples were identified by a unique identifier, which contains the nominal composition of the composite materials denoted by the nominal weight percentage of the mixed oxide with respect to the carbon content, along with the nominal molar ratio of Sn in the mixed oxide: e.g., 75Sn01 means the composite of 75 wt% $Ti_{0.9}Sn_{0.1}O_2$ – 25 wt% C.

It should be noted that in the preparation of composites with high carbon content (75 wt%) it is important to provide additional HNO_3 before starting the aging procedure to maintain the appropriate acidity of the synthesis mixture (for more details see Table 1).

In addition, our preliminary results demonstrated [81] that when preparing composite materials with the $Ti_{0.8}Mo_{0.2}O_2$/C= 25/75 ratio, aging the synthesis mixture at room temperature for 4 days is not always sufficient to prepare a pure TiO_2-rutile phase. The difference between the preparations of the 25Sn02 and 25Sn02–7 samples with high carbon content was the duration of the aging step, which was 4 and 7 days, respectively (see Figure S1 of the Supplementary Materials). Thus, the indication in the abbreviation of the 25Sn02–7 composite (see Table 1) means that the aging step is not the commonly used 4 days, but it is 7 days.

Composite support materials were loaded with 20 wt% Pt via a modified $NaBH_4$-assisted ethylene-glycol (EG) reduction-precipitation method (for details see ref. [82]).

The designation of the catalysts additionally indicates the support synthesis route (***A*** or ***B***): e.g., Pt/75Sn01/B means Pt catalyst supported on 75 wt% $Ti_{0.9}Sn_{0.1}O_2$–25 wt% C composite, which was prepared by synthesis route ***B***.

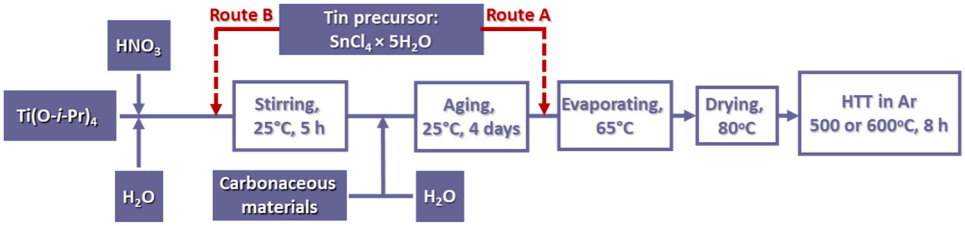

Fig. 1. Preparation steps of $Ti_{(1-x)}Sn_xO_2$–C composites with $Ti_{(1-x)}Sn_xO_2$/C= 75/25 mass ratio via routes ***A*** and ***B***; HTT: high-temperature treatment.

Table 1
Nominal composition and preparation details of the $Ti_{(1-x)}Sn_xO_2$–C (**C**: Black Pearls 2000) samples with the different Ti/Sn and $Ti_{(1-x)}Sn_xO_2$/C ratios.

Sample	Samples nominal composition	TiO_2 sol			Suspension of carbon			Sn prec[b] (g)
		H_2O (mL)	HNO_3 (mL)	Ti prec[a] (mL)	C (g)	H_2O (mL)	HNO_3 (mL)	
75Sn01	$75Ti_{0.9}Sn_{0.1}O_2$-25 C	23.47	2.628	2.298	0.25	10.0	-	0.3024
75Sn02	$75Ti_{0.8}Sn_{0.2}O_2$-25 C	19.29	2.160	1.889	0.25	10.0	-	0.5593
75Sn03	$75Ti_{0.7}Sn_{0.3}O_2$-25 C	15.18	1.760	1.539	0.25	10.0	0.090	0.7501
25Sn02	$25Ti_{0.8}Sn_{0.2}O_2$-75 C	6.43	0.72	0.630	0.75	24.1	1.441	0.1864
25Sn02–7[c]	$25Ti_{0.8}Sn_{0.2}O_2$-75 C	6.43	0.72	0.630	0.75	24.1	1.441	0.1864

[a] Ti precursor compound: titanium-isopropoxide (Ti(O-*i-Pr*)$_4$, 97%);
[b] Sn precursor compound: tin (IV) chloride pentahydrate ($SnCl_4 \times 5\ H_2O$, 98%);
[c] The duration of the aging step was 7 days.

2.3. Physicochemical characterization

X-ray powder diffraction (XRD) patterns were obtained in a Philips model PW 3710 based PW 1050 Bragg-Brentano parafocusing goniometer using CuKα radiation (λ= 0.15418 nm), graphite monochromator and proportional counter. Silicon powder (NIST SRM 640) was used as an internal standard. Lattice parameters were determined using a full profile fit (Pawley-fit) [86]. The cell parameters of the crystalline phases were determined from the fitted values.

Nitrogen physisorption measurements were carried out at temperature of liquid nitrogen using Thermo Scientific Surfer automatic volumetric adsorption analyzer (Thermo Fischer Scientific, Berlin, Germany). The specific surface area was calculated by the BET method in the range of relative pressures from 0.05 to 0.30.

Transmission Electron Microscopy (TEM) studies of the samples were made by use of a JEOL 2100 transmission electron microscope equipped with high resolution polar piece. In addition, the microstructure was also investigated by TEM using a FEI Titan Themis 200 kV C_s—corrected TEM with 0.09 nm HRTEM resolution. The structure has been identified by Selected Area Electron Diffraction (SAED). The scanning transmission electron microscopy (STEM) capabilities of the microscopes were utilized in recording of high resolution elemental maps by the energy dispersive X-ray spectrometry (EDS). Evaluation and processing of the high resolution micrographs was performed using the ImageJ software [87]. The samples for TEM analysis were prepared by dripping a few drops from the material suspension of the powder in ethanol on a microscopy grid with a carbon membrane.

Scanning Electron Microscopy (SEM) measurements on the samples were performed with a scanning electron microscope Vega II LMU model from Tescan (Brno, Czech Republic), equipped with an energy dispersive X-ray (EDX) spectrometer Bruker Quantax 200 (Bruker Physik-AG, Karlsruhe, Germany), at the following operational parameters: accelerating voltage 30 kV, measuring time 1200 s, working distance around 17 mm, counting rate 0.4 kcps.

Raman spectra were recorded on a LabRAM HR Evolution spectrometer from Horiba Jobin Yvon (HORIBA France SAS), with a laser radiation at wavelength of 633 nm. The spectra were recorded at room temperature in the extended scan mode in the 50–2000 cm^{-1} range.

X-ray photoelectron spectroscopy (XPS) measurements were performed using an EA 125 electron spectrometer manufactured by OMICRON Nanotechnology GmbH (Germany). MgKα (1253.6 eV) radiation was used as excitation source and data were acquired with 1 eV spectral resolution (30 eV pass energy). The powdered composite supports and catalysts were suspended in isopropanol and drops of this suspension were dried onto stainless steel sample plates. Spectra were processed with the CasaXPS package [88] by fitting the measured data with a combination of Gaussian-Lorentzian peaks using a Shirley-type background, while quantitative evaluation of the data was performed with the XPSMultiQuant package [89,90], during which a homogeneous depth distribution was assumed for all components as described in our previous studies. Chemical states were identified using the NIST database [91], the publication [92] or other literature as indicated. Binding energies were related to the lowest binding energy contribution of the C 1s envelope, which was assigned to graphite-like (sp^2-hybridized) carbon in the carbonaceous backbone (284.4 eV).

2.4. Electrochemical characterization

The measurements were performed in a conventional three-electrode electrochemical glass cell using a Biologic SP150 potentiostat and the EC-LAB software package. The applied electrolyte was 0.5 M H_2SO_4. The working glassy carbon (GC) electrode (d= 0.3 cm, geometric surface area A= 0.0707 cm^2) was polished before each test to remove any traces of organic impurities. The details of the catalyst ink composition and electrocatalytic measurements were described in our previous work [82]; the Pt loading of the electrodes was 10 μg cm^{-2}. Pt was used as counter electrode and the reference electrode was reversible hydrogen electrode (RHE). All potentials are given on RHE scale.

For CO_{ads}-stripping voltammetry, the electrolyte was saturated with CO for 30 min and then purged with Ar to remove CO dissolved in the electrolyte and physically adsorbed on the surface of the working electrode. Forward polarization from 50 mV to 1000 mV (vs. RHE) was applied with 10 mV s^{-1} scan rate.

Electrocatalytic performance of the Pt electrocatalysts was studied by cyclic voltammetry (CV) and CO_{ads}-stripping voltammetry measurements combined with stability test involving 500 polarization cycles and the second CO_{ads}-stripping voltammetry measurement. After stability test, the electrolyte was changed to fresh one to avoid the re-deposition of the dissolved metals. In the long-term stability test, the samples were submitted to cyclic polarization at a 100 mV s^{-1} scan rate for 10,000 cycles between 50 and 1000 mV potential limits (these measurements took about 54 hours).

The electrochemically active Pt surface area (ECSA) of the electrocatalysts was determined from cyclic voltammograms recorded by 10 mV s^{-1} scan rate between 50 and 1000 mV potential window. The charge required for oxidation of the underpotentially deposited hydrogen was calculated [93] using conventional baseline correction as described in our previous study [82].

The change of the electrochemically active surface area of Pt during the stability test after N cycles of polarization is presented as $ECSA_N$ (N: 500, 2500, 5000 and 10,000) normalized to $ECSA_1$ measured in the 1st cycle on the same sample ($ECSA_N/ECSA_1$). Thus, the loss in ECSA during N-cycle stability test ($\Delta ECSA_N$) was calculated from the charges originated from the hydrogen desorption in the 1st and N^{th} cycles according to the Eq. 1 [82]:

$$\Delta ECSA_N = \{1-(ECSA_N/ECSA_1)\}\times 100\% \quad (1)$$

Catalytic activity of the catalyst samples was tested in the ORR by rotating disc electrode (RDE) technique as described in our previous study [94]. The ORR measurements were done in O_2 saturated 0.5 M H_2SO_4 solution. The diameter of RDE electrode and Pt loading used in these experiments was the same as during CV measurements. Polarization curves were recorded by cathodic scan sweeping the potential between 1000 and 200 mV with 10 mV s^{-1} sweep rate, rotating the electrode at 225, 400, 625, 900, 1225 and 1600 revolutions min^{-1} (rpm).

Catalytic activity in the hydrogen oxidation reaction (HOR) was also investigated by RDE method in hydrogen saturated 0.5 M H_2SO_4 solution at 400, 625, 900, 1225 and 1600 rpm. Polarization curves were recorded by anodic scan sweeping the potential between 0 and 300 mV with 10 mV s^{-1} sweep rate. The diameter of RDE electrode and Pt loading used in these experiments was the same as during CV and ORR measurements.

Electrochemical performance of Sn-containing Pt electrocatalysts was compared with commercial reference 20 wt% Pt/C (Quintech).

3. Results and discussion

3.1. Comparison of the structural characteristics of the $Ti_{(1-x)}Sn_xO_2$–C composite support materials and related Pt electrocatalysts

The success of the synthesis of the Sn-doped TiO_2-based composites with different Ti/Sn ratios using either route ***A*** or ***B*** was confirmed by XRD measurements, which provide information on the phase composition of the samples. Diffraction patterns of the $Ti_{(1-x)}Sn_xO_2$–C (x: 0.1, 0.2 and 0.3) composite materials before and after the HTT and after Pt loading are shown in Fig. 2 (left panel: for route ***A***, right panel: for route ***B***), while the results of the measurements are summarized in Table 2.

The exclusive presence of rutile-type TiO_2 crystallites (with no indication of anatase TiO_2 phase) in the XRD patterns of the samples studied before HTT was demonstrated for both synthesis routes, although the crystallinity of the material from route ***A*** seems to be

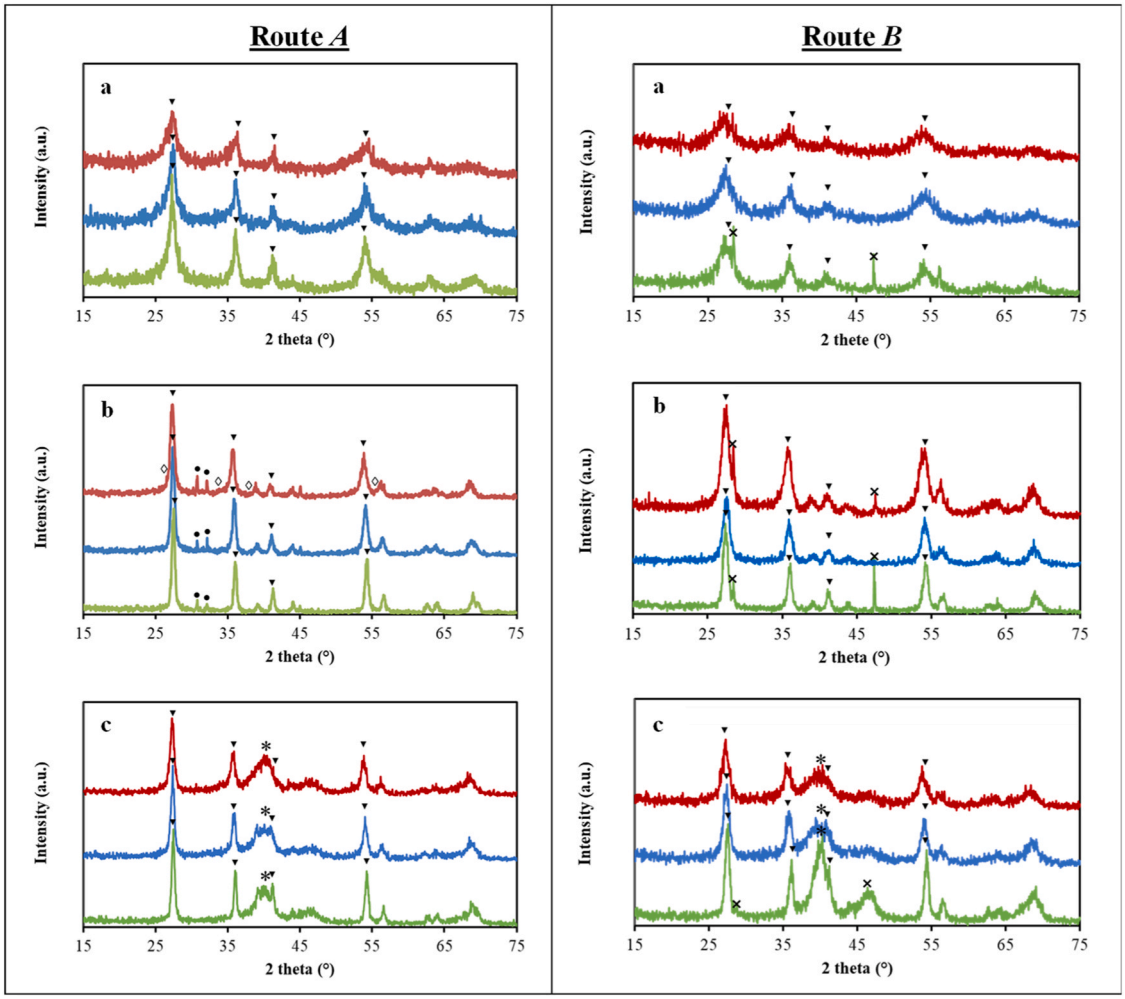

Fig. 2. XRD patterns of the Pt/75 wt% $Ti_{(1-x)}Sn_xO_2$–25 wt% C composite materials before (a) and after (b) HTT as well as after Pt loading (c). Synthesis route ***A*** (left panel) and route ***B*** (right panel): x= 0.1 (■), x= 0.2 (■) and x= 0.3 (■). ▼- Rutile, ●- Sn^0, ◇- SnO_2, *- Pt, ×- internal standard (Si: narrow reflections around 28° and 47°).

Table 2
Structural properties of the $Ti_{(1-x)}Sn_xO_2$–C composite materials prepared by routes ***A*** and ***B***.

Sample ID	S_{BET} (m^2/g)[a]	Total pore volume (cm^3/g)[b]	HTT (Phase, %)		attice parameters, Å[b]	$Sn_{subst.}$, %
			R/ nm	Sn^0/ SnO_2		
75Sn01/ A	374	0.95	99/ 29	1/0	*a*= 4.610, *c*= 2.970	7–8
75Sn02/ A	438	1.24	99/ 22	1/0	*a*= 4.620, *c*= 2.985	14
75Sn03/ A	390	0.66	95/ 20	2/3	*a*= 4.625, *c*= 2.988	23
75Sn01/ B	378	0.78	100/ 18	-	*a*= 4.608, *c*= 2.975	~9
75Sn02/ B	390	0.67	100/ 12	-	*a*= 4.610, *c*= 2.982	~10
75Sn03/ B	424	0.68	100/ 11	-	*a*= 4.625, *c*= 2.988	~25
25Sn02/ B	1185	1.77	100/ 9	-	*a*= 4.622, *c*= 3.004	~20
25Sn02/ B-7	1168	1.68	100/ 10	-	*a*= 4.622, *c*= 3.004	~20

[a] Specific surface area (S_{BET}) and total pore volume of the composite support materials determined by N_2 physisorption measurements;
[b] Lattice parameters of the rutile phase obtained after HTT (pure rutile TiO_2: *a*= 4.593 Å, *c*= 2.959 Å).

higher (see Fig. 2, subpanels ***a***).

After the HTT step, the changes in the lattice parameters (certain distortions compared to the pure rutile TiO_2 lattice parameters) obtained from the reflection angles confirmed the incorporation of tin into the TiO_2-rutile unit cell (see Table 2). The degree of Sn incorporation correlated with the amount of tin precursor. For $Ti_{(1-x)}Sn_xO_2$–C with x= 0.1, 0.2 and 0.3 the amount of tin in cation substitution position (Sn_{subst}) was 7, 14 and 23% for route ***A*** and 9, 10 and 25% for route ***B***. The slightly lower degree of Sn incorporation calculated for these samples compared to the nominal tin content may be an indication of the presence of disordered tin oxide species. Unfortunately, the relatively low signal-to-noise ratios made it difficult to accurately determine cell parameters, even in the presence of an internal standard, thus the uncertainty of these incorporation values is high, especially for the composites with low mixed oxide content.

At the same time, as shown in Fig. 2 (left panel, ***b***), the presence of a very small amount of metallic Sn (1–2%) after HTT was revealed in the samples prepared via route ***A***. Metallic tin can be formed as a result of carbothermal reduction of tin oxide [95]. It should be noted that very small reflections characteristic to Sn oxide were also found, but only in the composite with the highest nominal Sn content (see Fig. 2, left panel, ***b***). As shown in Fig. 2 (right panel, ***b***), such peculiarities were not detected in the composites prepared by route ***B***.

As demonstrated in Table 2, the oxide crystallite size was significantly higher for route ***A*** (20–29 nm), while route ***B*** resulted in relatively well-dispersed oxides (9–18 nm).

Actually, the formation of relatively small particles of Sn-doped TiO_2 oxide materials is consistent with the observation that the introduction of tin inhibits sintering of rutile crystallites during HTT [85].

After the deposition of Pt by a modified $NaBH_4$-assisted ethylene glycol reduction-precipitation method [80] (Fig. 2 (left panel, ***c***)), the reflections of the Sn^0 and SnO_2 phases completely disappeared for the composites from route ***A***. As shown in Fig. 2 (subpanels ***c***), in all Pt catalysts platinum was present in nanodispersed form, as evidenced by the small grain size estimated using the Scherrer formula (2.5–3.5 nm).

The presence of the typical TiO_2 rutile type Raman-active optical phonon modes and the absence of lines associated with the SnO_2 phase was also confirmed by Raman spectroscopy measurements performed on $Ti_{(1-x)}Sn_xO_2$–C (x: 0.1, 0.2 and 0.3) composite materials obtained via route ***A*** (see Figure S2 of the Supplementary Materials). As shown in Figure S2, these composite materials exhibit distinct Raman characteristics for both Ti–O–Ti bonds and C–C/C=C bonds with a high degree of distortion [96–98] (for more details see Chapter 2.1 in the Supplementary Materials).

According to the nitrogen physisorption measurements (see Table 2), the specific surface area (S_{BET}) of Sn-containing composites meets the requirements for promising electrocatalyst supports, which should be ≥ 100 $m^2\ g^{-1}$ [99]. S_{BET} and pore volume values of the composites prepared by route ***A*** are quite similar to those obtained by route ***B***. As can be seen from data in Table 2, in the case of using the same carbonaceous material the S_{BET} of $Ti_{(1-x)}Sn_xO_2$–C composites mainly depends on the mixed oxide-to-carbon ratio. As the content of carbonaceous material in composites increases, the S_{BET} also increases. It has to be mentioned that the S_{BET} of the parent Black Pearls 2000 carbon is 1635 $m^2\ g^{-1}$ [100].

TEM overview images of the 75 wt% $Ti_{(1-x)}Sn_xO_2$–25 wt% C composite materials with various Ti/Sn ratios prepared by route ***A*** are compared in Figure S3 (Supplementary Materials, top row), while higher magnification images are presented in Figure S4. A characteristic feature of the samples was the presence of nanorod-type larger crystallites (with length around 50–80 nm and width around 20 nm) often grouped into flower-like agglomerates, while small elongated or quasi-spherical oxide particles with sizes around 5–20 nm were more or less homogeneously mixed with carbon (Figure S4, Supplementary Information). The onion-like structure of the carbon material can also be well recognized. Electron diffraction confirmed that both the larger oxide elements and the smaller ones were predominantly rutile. The co-existence of large mixed oxide nanorods and much better dispersed oxide nanoparticles, resulting in a certain structural inhomogeneity of the composite, was also documented for the $Ti_{(1-x)}Mo_xO_2$-containing systems, especially for those containing higher amount of mixed oxide [82].

TEM images of the Pt/$Ti_{(1-x)}Sn_xO_2$–C (x: 0.1–0.3) electrocatalysts on supports prepared by route ***A*** are presented in Figure S3 (Supplementary Materials, bottom row). The morphological features of the non-platinized composites were well retained: the anisotropic rod-like oxide crystallites and their flower-like agglomerates were easily observable, while EDS analysis (not shown) demonstrated the presence of tin and titanium also in areas not covered by these large oxide assemblies. The latter regions can be identified as those containing a relatively homogeneous oxide-carbon mixture. The importance of the multidimensional structure formed by Pt/SnO_2 flowers, which enhances the electrode conductivity and leads to higher electrocatalytic activity and better long-term stability compared to the rod structure of Pt/SnO_2 and Pt/C, has been demonstrated in ref. [28].

Higher magnification micrographs of the Pt-loaded electrocatalysts on supports prepared by route ***A*** are shown in Fig. 3.

Pt nanoparticles can be observed as well dispersed, uniformly distributed 2–4 nm sized objects with dark contrast on the surface of all catalysts (see Fig. 3), in agreement with the XRD results (Fig. 2, left panel, ***c***). According to electron diffraction and measured lattice plane distances, these features were metallic Pt nanoparticles (Figure S5 (Supplementary Information) and Fig. 3). The Pt nanoparticles were uniformly distributed on both the large oxide features and on the more homogeneous regions. They were frequently associated with oxide elements (Figs. 3e and 3f), but were also present on seemingly oxide-free carbon regions (Fig. 3d). HRTEM images occasionally suggested the presence of very small oxide particles with brookite structure (Fig. 3e). In some cases Pt particles had a tendency to cluster on the large mixed oxide $TiSnO_x$ formations (see Fig. 3c).

HAADF image of the selected fragment of the Pt/75Sn02/A catalyst and EDS elemental maps obtained over this area are presented in Fig. 4a and b-c, respectively. As shown in Fig. 4b, the distributions of Ti, Sn and O elements were always closely correlated and the elemental ratios corresponded well to the expectations (Ti/Sn ~ 4:1 and Ti/O ~ 1:2). In addition, neither pure Ti nor pure Sn-containing features were detected. Usually, the $TiSnO_x$ was O-deficient. Elemental maps confirmed (see

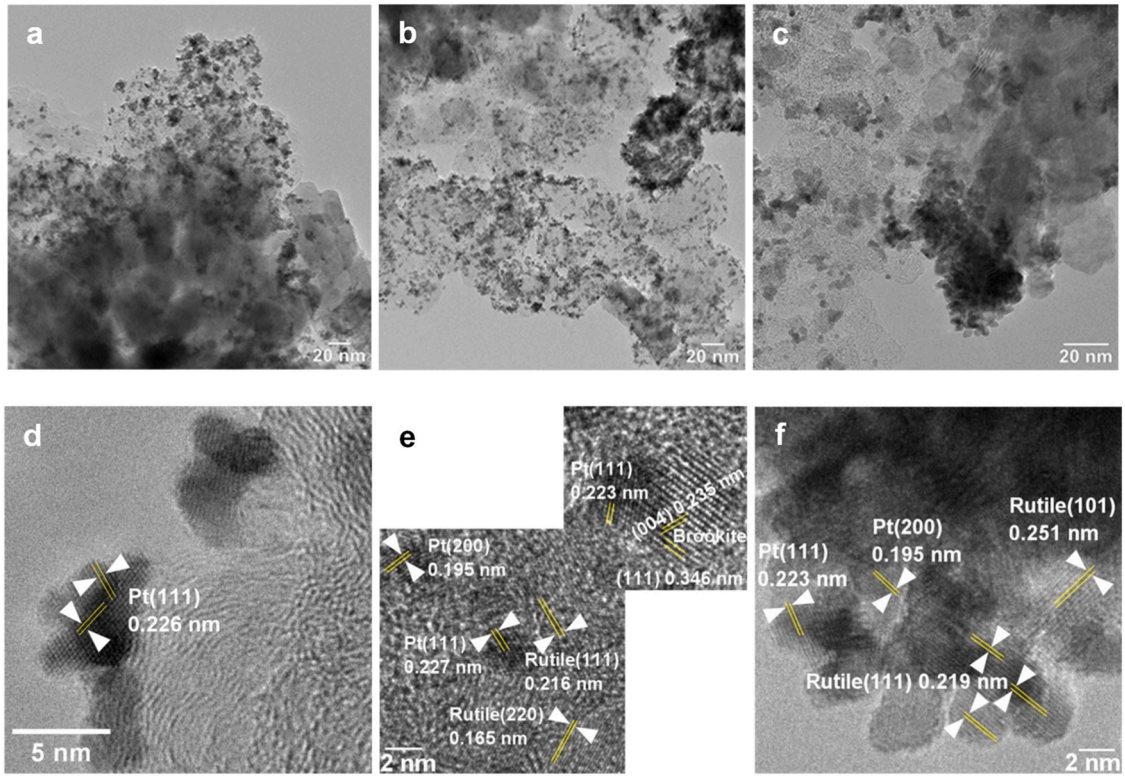

Fig. 3. TEM images of the Pt/75 wt% $Ti_{(1-x)}Sn_xO_2$–25 wt% C composite supported electrocatalysts prepared by route ***A***: x= 0.1 (a, d), x= 0.2 (b, e) and x= 0.3 (c, f).

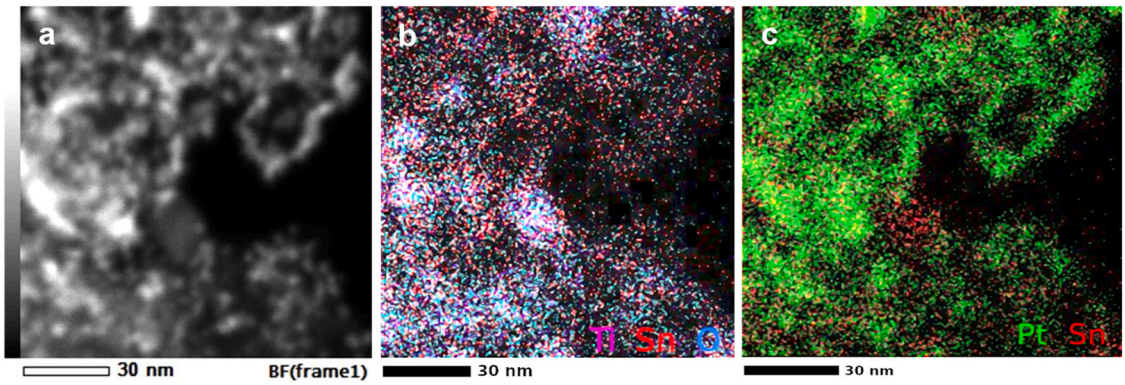

Fig. 4. HAADF image of the selected fragment of the Pt/75Sn02/A catalyst (a) and EDS elemental maps of Ti, Sn, O (b) and Pt, Sn elements (c) obtained over this area. Color code: Ti (pink), Sn (red), O (blue) and Pt (green).

Fig. 4c) that there are regions where Pt and the Sn doping element were located in close proximity to each other providing in this way surface ensemble sites suitable for bifunctional mechanism.

Figure S6 (Supplementary Materials) shows the HAADF images and STEM-EDS elemental maps of the selected fragment of the composite support material with Ti/Sn= 90/10 (top) and related Pt/75Sn01/A catalyst (bottom). In particular, Ti/Sn ratios measured by STEM-EDS on the nanorod-like crystallites or their flower-like agglomerates coincided very well with the nominal composition data (Ti/Sn ~ 9:1 and Ti/O ~ 1:2). However, it is not excluded that in composites prepared by route ***A*** certain amount of tin is also distributed over the carbon. The elemental distribution pattern of Pt in the Pt/75Sn01/A catalyst shown in Figure S6 (bottom) confirmed that Pt settled on both the large mixed oxide features and on the more homogeneous parts of the composite support.

In contrast with the systems prepared by route ***A***, the micrographs of the Pt electrocatalysts supported on composites prepared via route ***B*** revealed a much more homogeneous microstructure at both lower (Figure S7, Supplementary Materials) and higher (Fig. 5) magnifications.

A distinctive feature with respect to the materials obtained by route ***A*** was the lack of the nanorod-like oxide particles or the flower-like big $TiSnO_x$ agglomerates. Instead, faceted rutile particles in the 10–15 nm size range as well as weakly crystallized and/or graphitized C-rich regions were evidenced. The microstructure of the supports was quite similar; no effect of the different Ti/Sn ratios was obvious. The supports were covered by 2–3 nm metallic Pt particles as confirmed by electron diffraction and lattice spacing data (Figure S7 (Supplementary Materials) and Fig. 5). There was no correlation between the sizes of either the Pt or the oxide particles and the nominal tin content of the supports.

Micrograph of the Pt/75Sn02/B catalyst taken in HAADF mode along with the corresponding Pt, Sn and Ti elemental maps is shown in Fig. 6. As expected, Pt crystallites produced the strongest contrast in the HAADF image, but oxide particles were also easily observable. Tin was

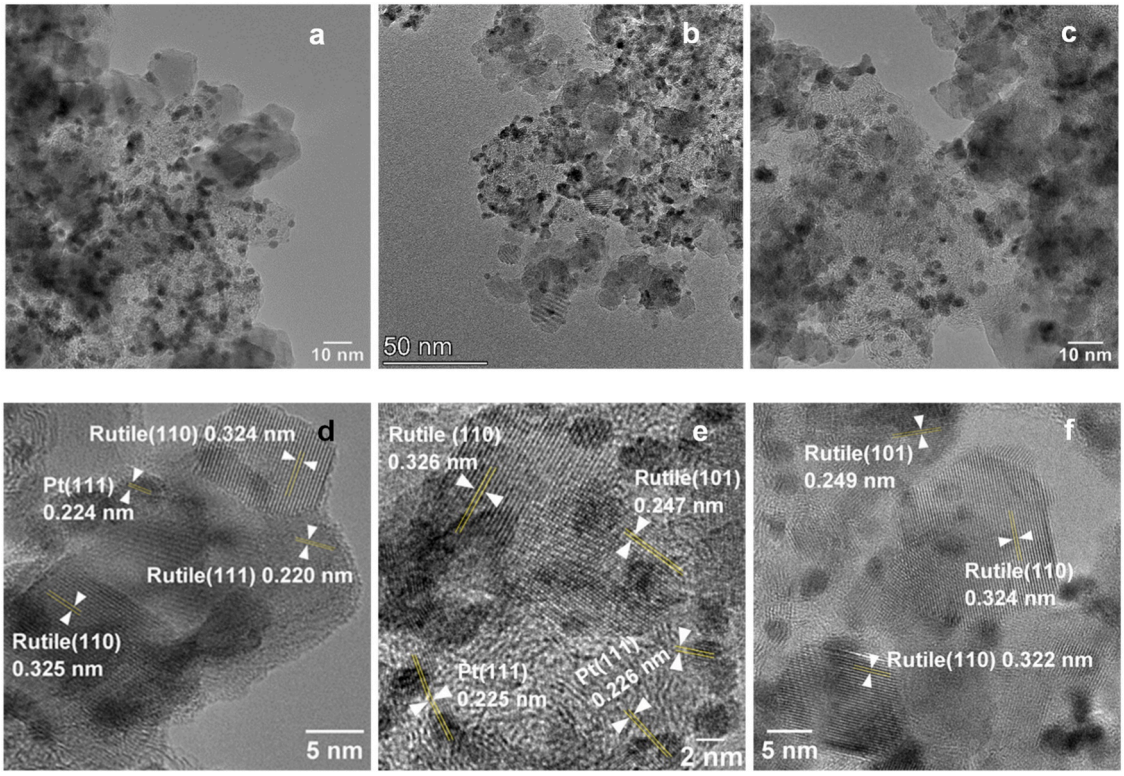

Fig. 5. TEM images of the Pt/75 wt% $Ti_{(1-x)}Sn_xO_2$–25 wt% C composite supported electrocatalysts prepared by route ***B***: x= 0.1 (a, d), x= 0.2 (b, e) and x= 0.3 (c, f).

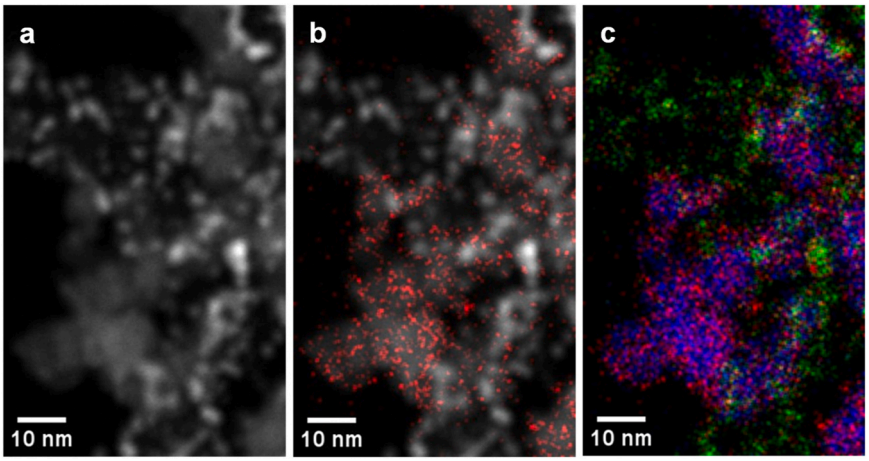

Fig. 6. (a) HAADF image of a selected fragment of the Pt/75Sn02/B catalyst, (b) overlay of the HAADF image and Sn elemental map as well as (c) elemental maps of Pt, Ti, and Sn obtained in this area. Color code: Ti (blue), Sn (red), and Pt (green).

almost exclusively detected in the oxide particles and its distribution was congruent with that of Ti or oxygen (not shown). Nevertheless, the edge of the oxide crystals was often dominated by tin signals, suggesting Sn enrichment at the surface of the particles.

Regarding the TEM image of the composite materials with high carbon content (75 wt%), even smaller mixed oxide nanoparticles with size lower than 10 nm were observed (Figure S8 of the Supplementary Materials). Taking into account the spatial distribution of oxide crystallites in these two samples, we can assume a fairly homogeneous oxide coating. The catalysts contained 2–3 nm size metallic Pt particles uniformly dispersed over the composite surface.

SEM/EDX technique was used for the investigation of the morphology of composite supported Pt electrocatalysts; selected results obtained on the $Pt/Ti_{0.8}Sn_{0.2}O_2$–C catalysts with high and low carbon content prepared using composites synthesized via route ***B*** are shown in Figure S9 (Supplementary Materials). EDX results obtained on $Pt/Ti_{(1-x)}Sn_xO_2$–C electrocatalysts are summarized in Table S1 in the Supplementary Materials (results obtained on composites prepared by route ***A*** are also included and reflect, to some extent, the significant inhomogeneity of these materials demonstrated by TEM). The main result of these investigations was that Ti/Sn ratios were quite close to the nominal values both in composites and Pt electrocatalysts. In fact, it is not surprising in case of the composites, since the method we used to prepare $Ti_{(1-x)}Sn_xO_2$–C supports does not involve steps where loss of tin or titanium would be expected (see Fig. 1). On the other hand, the minimal difference between the results presented in Table S1 and the nominal Ti/Sn values for Pt electrocatalysts, demonstrated the lack of partial dissolution of tin during Pt loading. This is in contrast with the

case of catalysts containing Mo, where dissolution of the less stable (not incorporated into the TiO_2 lattice) Mo species was noted during Pt loading [80].

Surface composition of selected supports and electrocatalysts was determined by XPS; the results are compared to the more bulk-sensitive EDX data in Table 3.

A general feature of the samples prepared by route ***A*** was that the surface oxide/carbon ratio strongly deviated from the nominal value: the apparent carbon content deduced from the XPS spectra was much higher than expected. EDX data (see Table 3) for composite materials indicated the same tendency although to a somewhat smaller extent. However, we have shown [94] that the Pt content obtained from the EDX data strongly depends on the areas chosen for analysis: thus, the Pt content in the catalysts is close to nominal only in mixed oxide-rich regions, and in carbon-rich areas less Pt is present. Therefore, EDX measurements of the Pt-loaded catalysts have usually focused on oxide-rich regions, and the resulting $TiSnO_x$/C mass ratio in the analyzed area is typically higher than the nominal value (for more details see Table S1 in the Supplementary Materials).

It should be noted that the phenomenon of unexpectedly high apparent surface carbon content (deduced from XPS) was also observed in the case of Mo-doped titania-carbon composites, especially at high nominal oxide contents and was traced to the co-existence of large, flower-like oxide agglomerates with much more dispersed ones, i.e., to the significant inhomogeneity of the composite [82,101]. TEM analysis of the composites prepared by route ***A*** indeed convincingly demonstrated this kind of inhomogeneity in the $Ti_{(1-x)}Sn_xO_2$–C systems.

In a supporting experiment, the formation of the large oxide agglomerates was traced to the high-temperature treatment. A 75Sn02/A composite without HTT was subjected to a simulated heat treatment between 300 °C and 600 °C in Ar in the preparation chamber of the electron spectrometer and the composition/surface chemistry changes were followed by XPS. The results are summarized in the first five rows of Table S2 in the Supplementary Materials. A larger change of the oxide/carbon ratio after the 300 °C annealing step suggested that the sintering of the oxide occurred already in the initial stage of the HTT; after higher-temperature steps, only much smaller increase of the apparent carbon content was seen. The Ti/Sn ratio indicated consistently very high but gradually decreasing tin excess. It has to be noted that neither the oxide/carbon ratio nor the Ti/Sn ratio changed too significantly between the 500 °C and 600 °C steps, while both treatments resulted in considerable reduction of the Sn content.

Composition results for composite supports and electrocatalysts obtained by route ***B*** are also summarized in Table 3.

In this case, very good agreement was experienced between the nominal and the apparent oxide/carbon ratio determined by XPS. The situation was similar concerning the Pt/support mass ratio in the studied electrocatalyst samples. In good agreement with the results demonstrated by TEM (see Fig. 5), this result suggests much better homogeneity of the samples on the length scale of the information depth of XPS (10 nm). Thus, much better oxide dispersion and/or coverage of carbon with less predominance of the flower-like aggregates is confirmed also by XPS, along with homogeneous distribution of the Pt particles.

A common feature of the composites prepared by route ***A*** and ***B*** was the very high surface tin content. While Ti/Sn ratios measured by EDX were close to the nominal values (see Table S1 or Table 3), the apparent Sn content found by XPS was much higher: in samples from route ***A*** it was equal to or even exceeded the Ti content. In comparison, in materials from support preparation route ***B***, the surface tin excess was clearly lower, suggesting a somewhat more homogeneous mixing of tin and titanium in the mixed oxide phase. Nevertheless, the nominal 4:1 Ti/Sn ratio was still not approached.

The significant tin excess can be explained by the surface enrichment of tin. Indeed, the high resolution elemental maps in Fig. 6 also suggested the formation of a tin-rich overlayer on the rutile particles.

The Ti/Sn ratios measured on the 75Sn02/A or 75Sn02/B composites and their platinized counterparts confirmed the lack of significant tis dissolution during Pt loading. As a result of the high surface concentration of Sn in these systems, significant influence of the Sn-Pt interactions on the electrocatalytic behavior can be expected.

It should be noted that the described behavior of tin is in a good agreement with the XPS observation of Sn-doped TiO_2 materials showing pronounced segregation of Sn on the rutile-TiO_2 surface and demonstrating a much bigger apparent tin surface concentration compared to the nominal bulk value [85]. Based on experimental data, it has been shown that surface tin enrichment is highest at low bulk doping levels and decreases at higher doping levels, indicating the saturation of surface sites with segregated dopant.

The thermal stability of the 75Sn02/B composite was also investigated in a supporting experiment consisting of simulated HTT in Ar in the electron spectrometer between 500 °C and 700 °C (see Table S2). Up to 600 °C, practically no change occurred in the apparent oxide/carbon ratio, which can probably be explained by the stabilizing effect of the Ti-Sn mixing against oxide sintering during HTT. This behavior is in clear contrast with the composites prepared by route ***A***, where oxide sintering was evident already after HTT at 300 °C-400 °C. Nevertheless, a slight but clear decrease of the oxide content of the 75Sn02/B composite after annealing to 700 °C in Ar indicated that HTT above 600 °C may not be advisable.

Fig. 7 compares the changes of the Sn 3d spectra of the 75Sn02/A and the 75Sn02/B composites during the simulated HTT series mentioned above. The dominant chemical state in both cases was Sn^{4+} with the Sn $3d_{5/2}$ peak around 487.0 eV [91,92,102]. Nevertheless, above a certain temperature, the appearance of a weak metallic signal at 484.8–485.0 eV indicated the onset of tin reduction. However, once

Table 3
Surface composition data obtained by XPS and EDX on selected samples containing composites prepared by routes ***A*** and ***B***.

Sample ID	Ti/Sn (at/at)			Sn^0[b]	$TiSnO_x$/C (wt%/wt%)			Pt/support (wt%/wt%)	
	Nom[a]	EDX	XPS		Nom[a]	EDX	XPS[c]	EDX	XPS
Route A									
75Sn02/A[d]	4/1	5.8:1	1.17:1	10%	75/25	59/41	52/48	–	–
Pt/75Sn01/A	9/1	11.8:1	0.75:1	3%	75/25	82/180[e]	55/45	22.1/77.9	27/73
Pt/75Sn02/A	4/1	5.5:1	0.57:1	3%	75/25	84/16[e]	57/43	18.6/81.4	31/68
Route B									
75Sn02/B	4/1	n.a.	1.62:1	<1%	75/25	n.a	73/27	–	–
Pt/75Sn02/B	4/1	5.1:1	2.05:1	<2%	75/25	91/9[e)]	82/18	21/79	21/79
Pt/25Sn02/B	4/1	5.1:1	1.83:1	3%	25/75	46/54[e]	24/76	21/79	21/79

[a] Nom: nominal values;
[b] Sn^0 fraction with respect to the total tin content; values of 2–3% are at the detection limit;
[c] Calculated without the Pt content;
[d] Data estimated from the results of the 600 °C step of the *in situ* simulated HTT series in the electron spectrometer;
[e] EDX studies have focused on regions rich in mixed oxides, so the carbon content data is significantly lower than nominal.

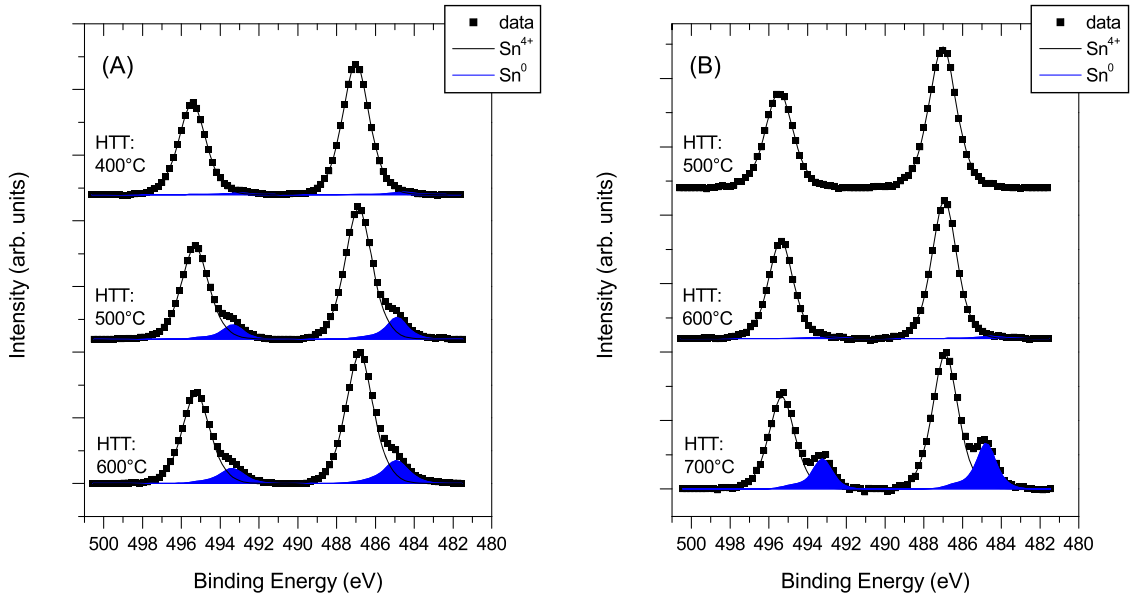

Fig. 7. Sn 3d spectra of the 75Sn02/A (A) and the 75Sn02/B (B) composites during simulated HTT in 300 mbar Ar in the electron spectrometer. Please note the difference in the temperature range.

again the much better stability of the support prepared by route ***B*** was evident: while the carbothermal reduction started around 400 °C and became quite significant after HTT at 500 °C in 75Sn02/A, the amount of metallic tin was undetectably small after 500 °C and remained marginal after 600 °C HTT in 75Sn02/B. Nevertheless, annealing of the latter composite above 600 °C resulted in strong reduction. This observation was taken into account when setting the HTT temperature of the supports prepared by route ***B*** to 500 °C.

The simulated HTT experiments of the 75Sn02/A and the 75Sn02/B composites confirmed the lack of significant structural rearrangements in the 500–600 °C range in both systems. Therefore, decreasing of the HTT temperature in the systems prepared by route ***B*** does not compromise the comparability with supports prepared by route ***A***.

Although the vast majority of tin was in the Sn^{4+} state both in the 75Sn02/A composite and the two electrocatalysts on supports from route ***A*** (Table 3), a small metallic contribution was evident in all cases. It should be noted that the data for the non-platinized composite were collected during the simulated HTT experiment, thus they represent a different situation than the air-exposed case obtained after the regular HTT. While the XPS results on the presence of metallic tin are in qualitative agreement with XRD observations made on the non-platinized composites, the much larger metallic Sn content found by XPS is probably due to the lack of air exposure. As metallic tin was present already in the non-platinized composites, it is difficult to determine how appearance of metallic tin in the Pt-loaded electrocatalysts is related to direct Pt-Sn interactions (i.e., the very easy reducibility of tin in atomic closeness to Pt [103]), which may play a role in the formation of the traces of reduced tin species in systems prepared via route ***B*** (see Table 3).

In summary, physicochemical characterization revealed significant structural differences between the composites obtained by routes ***A*** and ***B***. The composite material prepared via route ***A*** had inhomogeneous microstructure, resulting in coexistence of $TiSnO_x$ agglomerated into large flower-like clusters and a more uniformly distributed nanosized oxide, while in the 75Sn02/B composite the formation of relatively small particles of Sn-doped TiO_2 oxide materials was evidenced, which is consistent with the observation that the introduction of tin inhibits sintering of rutile crystallites during HTT. Both materials contained significant excess of ionic tin on their surface, although this tin excess was more stable against carbothermal reduction in case of the systems prepared by route ***B***.

3.2. *Electrocatalytic properties*

3.2.1. *Electrochemical behavior of the electrocatalysts prepared by route A*

Based on the obtained results (high degree of Sn incorporation, required S_{BET}, uniformly distributed 2–4 nm sized Pt nanoparticles) there is reason to assume that the obtained composites could serve as promising supports for Pt electrocatalysts.

Since one of our goals is to check the effect of Sn, used as a doping metal in the composite, on the electrochemical behavior of Pt/$Ti_{(1-x)}Sn_xO_2$–C electrocatalysts with different Sn content (x: 0.1–0.3), first the catalysts prepared by route ***A*** were investigated using CV, CO_{ads} stripping voltammetry and short (500-cycle) stability test performed by continuous cycling between 50 and 1000 mV potential limits (see Table 4 and Fig. 8).

As demonstrated in Fig. 8a, $Ti_{(1-x)}Sn_xO_2$–C composite supported Pt electrocatalyst showed enhanced CO tolerance: the CO started to be oxidized at about $E_{CO,onset}$= 200 mV. The position of the maximum of the main CO oxidation peak observed on the CO_{ads} stripping curves for various Pt/$Ti_{(1-x)}Sn_xO_2$–C electrocatalysts is summarized in Table 4. On Sn-containing composite supported catalysts two overlapping CO_{ads}-

Table 4
Electrochemical performance of the $Ti_{(1-x)}Sn_xO_2$–C composite supported 20 wt% Pt electrocatalysts.

Sample	$E_{CO,max}$, mV[a]	$ECSA_1$, m^2/g_{Pt}[b]	$\Delta ECSA_{500}$, %[c]	$\Delta ECSA_{10,000}$, %[c]
Pt/75Sn01/A	765 (*sh*: 705)	32.7 ± 2.5	7.5	39.0
Pt/75Sn02/A	775 (*sh*: 705)	33.6 ± 2.4	9.2	50.8
Pt/75Sn03/A	765 (*sh*: 705)	31.6 ± 2.7	16.6	n.m.
Pt/75Sn01/B	785 (*sh*: 675)	58.5 ± 1.4	7.3	42.7
Pt/75Sn02/B	775 (*sh*: 675)	59.3 ± 3.0	9.1	49.8
Pt/75Sn03/B	775 (*sh*: 675)	54.6 ± 1.8	16.7	n.m.
Pt/25Sn02/B	775 (*sh*: 435, 675)	68.7 ± 1.0	12.9	45.8
Pt/25Sn02/B-7	775 (*sh*: 435, 675)	78.2 ± 1.0	11.8	36.5
Pt/C	795	87.2 ± 2.3	12.7	47.8

sh= shoulder; n.m.: not measured.
[a] The position of the main CO stripping peak measured on fresh catalysts;
[b] The average $ECSA_1$ value obtained on fresh catalysts in four parallel measurements;
[c] $\Delta ECSA_{500}$ and $\Delta ECSA_{10,000}$ were calculated from the charges originated from the hydrogen desorption in the 1st and 500th or 10,000th cycles according to the Eq. 1 (see Experimental part);

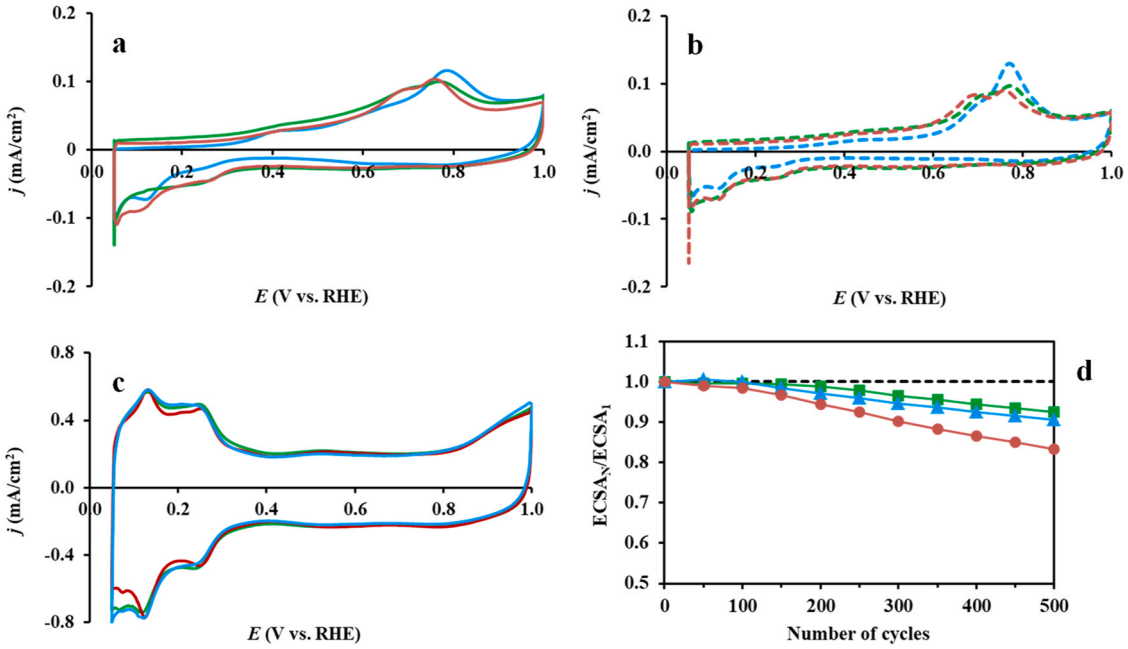

Fig. 8. Effect of the Ti/Sn ratios in $Ti_{(1-x)}Sn_xO_2$–C composite materials on the electrochemical performance of the catalysts prepared by route ***A***. CO_{ads} stripping voltammograms of the electrocatalysts obtained (a) before and (b) after the 500-cycle stability test; (c) CVs of the fresh electrocatalysts, and (d) ECSA change during 500 CV cycles: comparison of the ECSA measured after N cycles normalized to ECSA measured in the 1st cycle ($ECSA_N/ECSA_1$) of the Pt/75Sn01/A (■), Pt/75Sn02/A (■) and Pt/75Sn03/A (■) catalysts as a function of the number of cycles (N). Recorded in 0.5 M H_2SO_4 at 10 $mV{\cdot}s^{-1}$ (a, b) and 100 $mV{\cdot}s^{-1}$ (c), T= 25 °C.

electrooxidation peaks at around 705 and 765–775 mV were observed (see Fig. 8a and Table 4). Our previous study showed that on the reference Pt/C catalyst, the main CO_{ads} stripping peak is located at a more positive potential (ca. 795 mV [82]), but, for example, on Sn-Pt/C alloy-type catalysts CO electrooxidation occurs at ~ 700 mV [103].

It should be noted that, compared to our catalytic systems, oxidation of CO on the $Pt/Ti_{0.9}Sn_{0.1}O_2$–C catalyst of similar composition, prepared by the mixing of mixed oxide with Vulcan XC-72 carbon black [78], commences at much more positive potentials ($E_{CO,onset}$= 707 mV).

Somewhat surprisingly, the electrochemical performance of the electrocatalysts did not depend on the nominal Ti/Sn ratio in composite materials. The CO_{ads} stripping voltammograms obtained on the different catalysts were very similar; the observed difference is within the reproducibility of electrochemical measurements (see Fig. 8a). The possible reason for this behavior is the presence of a segregated tin oxide surface layer. Indeed, XPS indicated a very high apparent surface tin content (see Table 3), which correlated only weakly with the nominal tin content, suggesting the formation of such an overlayer in all catalysts. Thus, the Pt-tin oxide connections responsible for the CO tolerance can be equally abundant, regardless of the nominal Ti/Sn ratio. Moreover, the low $E_{CO,onset}$ value indicates that compared to the $Ti_{0.9}Sn_{0.1}O_2$-containing Pt electrocatalysts presented in ref. [78], this preparation method provides a significantly larger number of specific Pt sites, where Pt and Sn atoms are in atomic proximity. Accordingly, the electrochemical behavior of the catalysts prepared via route ***A*** reflected the known characteristics of SnO_x–containing Pt systems, confirming the importance of direct Pt-Sn interactions for improving catalytic activity.

In some cases, after 500 cycles of the stability test, a small shift (ca. 10 mV) of the main CO stripping peak can be observed toward less positive potential values compared to that obtained over fresh samples (see Pt/75Sn02/A sample in Fig. 8b). This kind of shift can be an indication of slight agglomeration of Pt nanoparticles [104]. However, it should be emphasized that TiO_2-based catalytic systems, due to the strong interaction between the titania and the Pt nanoparticles, usually have increased stability [105,106].

In the cyclic voltammograms of Fig. 8c, the region between 50 and 350 mV contains the typical adsorption/desorption peaks of underpotentially deposited hydrogen on the Pt surface. As can be seen from Fig. 8c, the shape of the CVs obtained on catalysts with different Sn contents was very similar (voltammograms were almost congruent and overlapped each other); the same trend was observed with the CO_{ads} stripping voltammograms (see above for explanation).

It should be noted that the electrochemical double-layer region remained practically unchanged during prolonged polarization (not shown), indicating good stability of the Sn-containing composite support materials. However, as shown in Fig. 8d, the stability of the Sn-containing composite supported Pt electrocatalysts decreased with increasing tin content in the composite materials. A similar tendency was observed on Mo-containing 20 wt% Pt/75 wt% $Ti_{(1-x)}Mo_xO_2$–25 wt % C catalysts with Ti/Mo= 80/20, 70/30 and 60/40 ratios [80].

Thus, the technique we developed for Mo-containing composite materials (route ***A***) can also be used for the preparation of Sn-containing composites demonstrating good stability. However, this method and the composites obtained in this way had the following drawbacks: (i) the formation of a small amount of metallic Sn phase, which disappears after Pt deposition, (ii) certain inhomogeneity of the composite materials (the formation of $TiSnO_x$ agglomerated in flower-like clusters), and (iii) relatively low electrochemically active Pt surface area of the catalysts (~30 $m^2\ g_{Pt}^{-1}$).

To avoid these issues, the synthesis of the composite was modified: the alternative route ***B*** was introduced (Fig. 1, route ***B***) and the final temperature of the HTT was decreased as described above.

3.2.2. *Electrochemical behavior of the electrocatalysts prepared by route B*

Influence of the order of adding tin precursor compound during the synthesis of composite materials along the route ***A*** and ***B*** on the electrochemical characteristics was demonstrated on Fig. 9.

As can be seen from Fig. 9, mixing Sn and Ti precursors prior to the addition of carbon resulted in a marked increase in both the ECSA of Pt (Fig. 9a) and CO electrooxidation peaks (Fig. 9c). However, as can be seen from Fig. 9c, this did not affect the position of the maximum of the CO oxidation peaks in the voltammograms. It can be assumed that similar active centers are formed during the preparation of composites by both methods, but the surface concentration of these centers in the

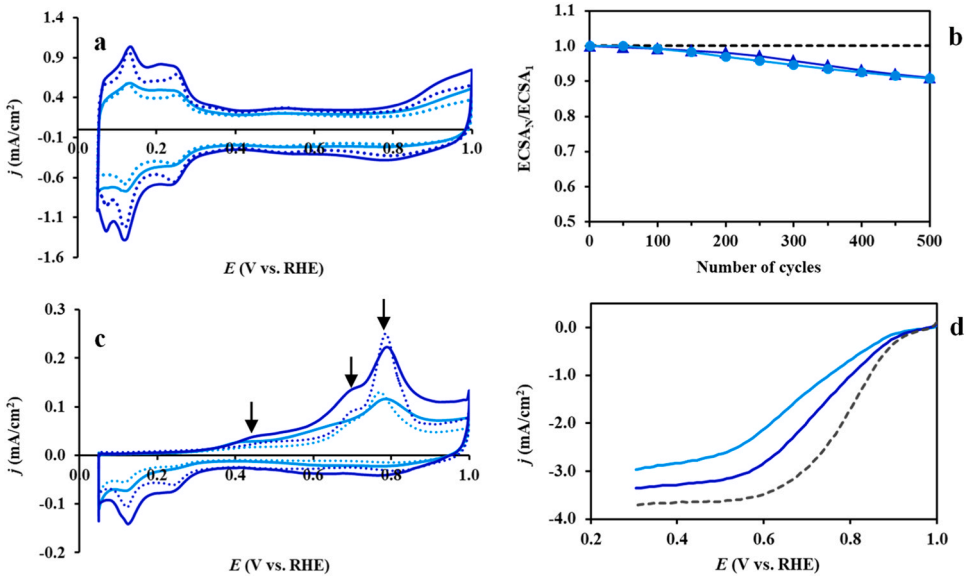

Fig. 9. Influence of the preparation method of composite materials on electrochemical performance of the Pt/75Sn02/A (■) and Pt/75Sn02/B (■) electrocatalysts: (a) CVs, (b) ECSA change during 500 CV cycles, (c) CO_{ads} stripping voltammograms, and (d) results of the RDE measurements at 900 rpm in ORR (the reference Pt/C (■) was included for comparison). The voltammograms were recorded in 0.5 M H_2SO_4 before (solid curves) and after 500 cycles (dotted curves) of the stability test. Sweep rate: (a) 100 mV·s^{-1} and (c, d) 10 mV·s^{-1}, T= 25 °C.

composites obtained by synthesis route ***B*** is higher. As shown in Fig. 9b, the decrease of the ECSA over 500 polarization cycles on catalysts prepared from a composite prepared by different synthesis routes (***A*** or ***B***) with the same Ti/Sn ratio was very similar. As emerges from Table 4, on catalysts with Ti/Sn ratio of 80/20, the loss of the ECSA after the 500-cycle stability test ($\Delta ECSA_{500}$) was about 9%. This indicates good stability of tin-containing catalysts, regardless of the method of preparing the composite (***A*** or ***B***).

Fig. 9d compares the electrocatalytic activity in the ORR of Pt/75Sn02 catalysts prepared by route ***A*** and ***B*** measured by RDE technique at 900 rpm in O_2-saturated 0.5 M H_2SO_4 solution; for comparison, the behavior in this reaction of a commercial reference Pt/C catalyst was also shown under similar conditions. As shown in Fig. 9d, the activity of the Pt/75Sn02/B catalyst was superior to that of the Pt/75Sn02/A, but the ORR current density in the mixed kinetic-diffusion controlled region on the fresh reference Pt/C catalyst was higher compared to the composite supported Pt catalysts with 75 wt% mixed oxide. According to the literature, the lower limiting current density, which is usually observed on oxide-containing catalysts, can be explained by the slower diffusion of oxygen through the oxide layer covering Pt nanoparticles [107,108].

In addition, as can be seen from Table 4, the ECSA values of the electrocatalysts prepared by route ***B*** were approximately two times higher compared to the catalysts synthesized by route ***A***. Thus, the electrocatalytic behavior of catalysts prepared using composite materials obtained by a new synthesis route based on thorough mixing of Ti and Sn precursors before the addition of the carbon (route ***B***) is in all respects superior compared to the activity of catalysts prepared with composites synthesized by route ***A***.

As shown in Figure S10 of the Supplementary Materials, similar to the results obtained with the catalysts prepared via route ***A***, there is practically no difference in the behavior of electrocatalysts with various Ti/Sn ratios containing composites synthesized by route ***B***: the CO_{ads} stripping voltammograms recorded before and after stability test (Figures S10a and S10b, respectively) and CVs (Figure S10c) obtained on different catalysts were almost identical and overlapped each other. It should be noted that the observed difference is within the reproducibility of electrochemical measurements (see Figure S10, Supplementary Materials). The slightly smaller peak maximum obtained for the catalyst with the highest tin content correlates well with the smaller ECSA value measured in comparison to the other two catalysts. In addition, the diluting effect of tin in Sn-Pt surface alloys leads to a decrease in the concentration of bridge bonded CO, and the diminishing back-donation from the Pt d-orbitals to non-bonding orbitals of CO results in weaker adsorption of linearly bonded CO, too [109]. The change in the electronic ligand effects eventually leads to a shift of the shoulder and the main CO peak towards slightly smaller positive values and a decrease in their intensity.

As can be seen from Figure S10d, in good agreement with the results obtained on the catalysts obtained via route ***A***, increasing the tin content in the composite materials leads to a decrease in the stability of Sn-containing electrocatalysts. This was the reason why 10,000-cycle long-term stability experiments were not carried out on catalysts with a Ti/Sn ratio of 70/30.

Effect of $TiSnO_x$/C mass ratio on the electrochemical performance of the electrocatalysts with low (25 wt%) and high carbon content (75 wt%) was presented in Fig. 10. Moreover, the effect of the duration of the aging step (4 or 7 days) used during preparation of composite with a high carbon content (75 wt%) via route ***B*** (see Figure S1, Supplementary Materials) on the electrocatalysts performance was also included (compare the behavior of the Pt/25Sn02/B and Pt/25Sn02/B-7 samples). As can be seen from Fig. 10a, the increase of the carbon content in composite materials leads to the following increase of the ECSA of Pt in related catalysts. In particular, the shape of the voltammograms and ECSA values (see Table 4) are comparable to those mentioned in the literature for Pt/$Ti_{0.9}Sn_{0.1}O_2$–C catalyst with oxide/carbon mass ratio of 30/70 (68.9 m^2 g^{-1}) [78].

As shown in Fig. 10c, the position of the maximum of the CO oxidation peaks on the voltammograms is independent of both the aging step duration (4 or 7 days) and the $TiSnO_x$/C mass ratio. Based on these results, it can be assumed that the increase in the carbon content in the composite materials prepared by route ***B*** leads to a further increase of the number of catalytically active sites responsible for enhanced CO tolerance. In this regard, it should be emphasized that among the prepared series of samples, catalysts with a carbon content of 75 wt% have the most homogeneous structure of the oxide coating on the carbon backbone. According to the literature, CO oxidation and ORR on Sn-containing electrocatalysts follow a bifunctional mechanism in which Sn sites provide OH_{ads} species at less positive potentials than the active

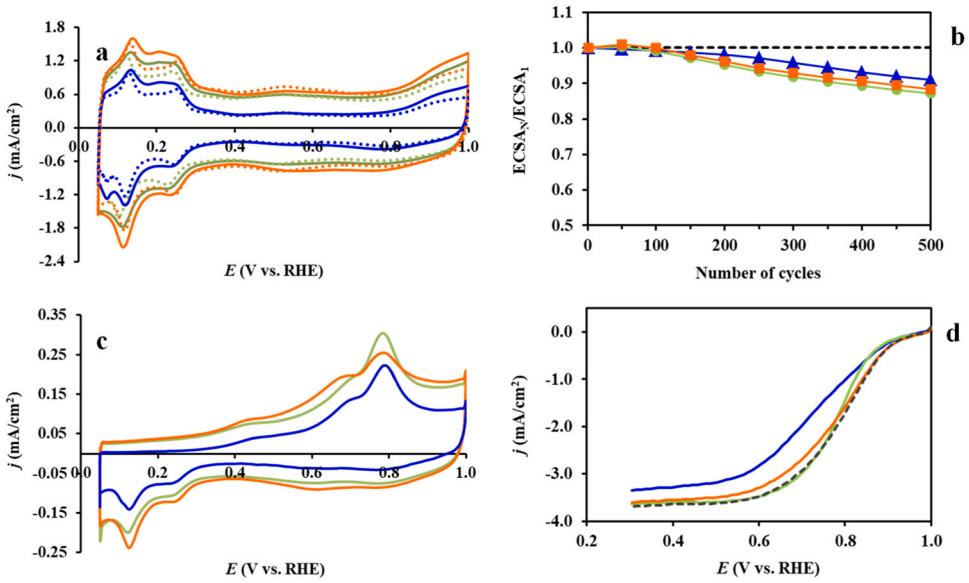

Fig. 10. Effect of $TiSnO_x$/C mass ratio on the electrochemical performance of the Pt/75Sn02/B (■), Pt/25Sn02/B (■) and Pt/25Sn02/B-7 (■) electrocatalyst with prolonged aging step: (a) CVs, (b) ECSA change during 500 CV cycles, (c) CO_{ads} stripping voltammograms, and (d) results of the RDE measurements at 900 rpm in ORR (the reference Pt/C (■) was included for comparison). The CVs were recorded in 0.5 M H_2SO_4 before (solid curves) and after 500 cycles (dotted curves) of the stability test. Sweep rate: (a) 100 mV·s^{-1} and (c, d) 10 mV·s^{-1}, T= 25 °C.

metal [36,37,40,99], or the surface SnO_x species participate in the chemisorption of O_2 as O^{2-}, which is the first and limiting step of the ORR [29].

In our recent study, it has been demonstrated [82] that the position of the main CO_{ads} stripping peak on 20 wt% Pt/$Ti_{0.8}Mo_{0.2}O_2$-C catalysts with 75 wt% mixed oxide in composite (705 mV) was shifted towards less positive potentials by 70 mV with respect to the main peak observed on the catalysts with 75 wt% carbon (775 mV). However, in contrast to systems containing Mo, results obtained on Sn-containing composite supported catalysts show that the peaks position in the CO_{ads} stripping voltammograms is independent of the mixed oxide/carbon ratio.

As can be seen from Fig. 10b, increasing the carbon content of the catalyst leads to an insignificant decrease in short-term stability compared to the Pt/75Sn02/B.

The comparison of the results of the RDE measurements obtained at 900 rpm in the ORR on the reference Pt/C and electrocatalysts with low (25 wt%) and high carbon content (75 wt%) prepared by route ***B*** was presented in Fig. 10d; the effect of the duration of the aging step (4 or 7 days) used in composite preparation on the performance of catalysts in the ORR was also demonstrated. Potentiodynamic (10 mV s^{-1}, negative sweep) oxygen reduction current densities obtained in O_2-saturated 0.5 M H_2SO_4 at six rotation rates on the catalysts presented in Fig. 10d were compared on Figure S11 (Supplementary Materials). The expected current density increase in the potential dynamic polarization curves at higher rotation rates (see Figure S11) was demonstrated for all catalysts, indicating faster diffusion of oxygen to the surface of catalysts.

As already noted above, the presence of a high content of mixed oxide (75 wt%) in catalysts negatively affects the activity in the ORR compared to the reference carbon supported Pt catalyst. However, as shown in Fig. 10d, the difference between the reference Pt/C and two catalysts with 25 wt% mixed oxide almost disappears. Thus, based on the results of these measurements, we can conclude that among the studied Sn-containing catalytic systems, electrocatalysts with a high carbon content (75 wt%) prepared by route ***B*** are the most promising.

The activity of these catalysts is comparable to the results obtained on the Pt/$Ti_{0.7}Mo_{0.3}O_2$ catalytic system, where the increased activity compared to Pt/C was explained by the presence of electronic synergistic interaction between Pt and $Ti_{0.7}Mo_{0.3}O_2$ support [55].

The influence of the preparation route used for composite support materials synthesis (***A*** or ***B***) and the effect of the $TiSnO_x$/C mass ratio in the composite on the loss of the ECSA during the 10,000-cycle stability test were compared in Fig. 11. The values of the electrochemically active Pt surface area loss ($\Delta ECSA_{10,000}$) were also included in Table 4.

As shown in Fig. 11a, in long-term stability tests over 10,000 cycles, comparable stability was obtained on electrocatalysts with the same composition. In this series of experiments, the best stability was obtained on a catalyst with high carbon content prepared with an aging step of 7 days (see Pt/25Sn02/B-7 sample in Table 4 and Fig. 11b).

Comparison of the electrocatalytic characteristics of Mo- and Sn-containing 20 wt% Pt/$Ti_{0.8}M_{0.2}O_2$–C (M: Mo, Sn) electrocatalysts with a high carbon content (75 wt%) was presented in Figure S12 (Supplementary Materials). For this purpose, a well-characterized Pt/$Ti_{0.8}Mo_{0.2}O_2$–C electrocatalyst with a mixed oxide/carbon ratio of 25/75, which was recently developed by us [82,94] was selected.

As shown in Figure S12 of the Supplementary Materials, the Mo- and Sn-containing electrocatalysts were compared by means of CV (Figure S12c) and CO_{ad} stripping voltammetry (Figure S12a) completed by 500-cycles stability test (Figure S12d) and the second CO_{ads}-stripping measurement (Figure S12b). In addition, electrocatalytic activity of these samples was also tested in the ORR (Figure S12e) and the HOR (Figure S12f). The results of these measurements show that the activity and stability of the novel tin-containing catalyst match or in some cases even exceed (e.g., ORR activity) the performance of the molybdenum-containing catalyst. This comparison shows that Sn-containing electrocatalysts can be not only promising CO-tolerant anode electrodes but also cathode catalysts for potential use in PEM fuel cells.

4. Conclusions

Comparison of two techniques for preparation of tin-containing $Ti_{(1-x)}Sn_xO_2$–C (x= 0.1, 0.2 and 0.3) composites, one being the adaption of the method previously developed for Mo-containing composite materials (route ***A***), and another modified by the simultaneous introduction of the precursors of Sn and Ti at the beginning of the synthesis (route ***B***), revealed very significant structural differences between the electrocatalyst supports obtained by the two routes. XRD, nitrogen physisorption measurements, TEM, SEM/EDX, XPS and Raman spectroscopy were used to characterize the bulk and surface microstructure of the

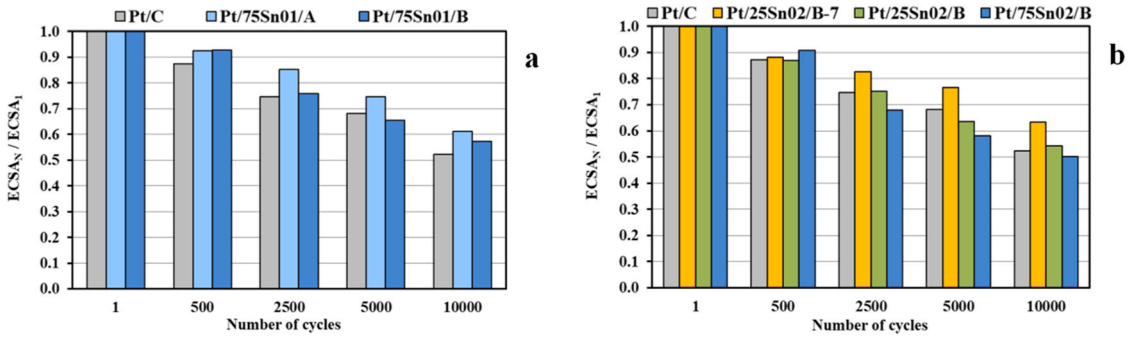

Fig. 11. ECSA change during 10,000 CV cycles: comparison of the ECSA measured after N cycles normalized to ECSA measured in the 1st cycle ($ECSA_N/ECSA_1$) as a function of the number of cycles (N): (a) influence of the preparation method, and (b) effect of $TiSnO_x$/C mass ratio in composite materials.

composites and their Pt-loaded counterparts. The change in the TiO_2 lattice parameters measured after HTT by XRD confirmed the incorporation of tin into the rutile unit cell for both synthesis routes and the degree of Sn incorporation was in good accordance with the amount of tin precursor. However, the composite materials prepared via route ***A*** had metallic Sn in a small amount (1–2%) and an inhomogeneous microstructure, expressed in the coexistence of $TiSnO_x$ agglomerated into large flower-like clusters and a more uniformly distributed nano-sized oxide. In addition, after Pt loading, electrocatalysts exhibited relatively low ECSA (~30 $m^2\ g_{Pt}^{-1}$). On the contrary, composites and Pt electrocatalysts obtained via synthesis route ***B*** did not contain segregated Sn^0 or SnO_2 phases, had a more homogeneous/uniform distribution of mixed oxide, and the ECSA values were comparable to those obtained on Mo-containing composite supported Pt catalysts with similar composition (~60–80 $m^2\ g_{Pt}^{-1}$).

A common feature of the composites prepared by routes ***A*** and ***B*** was the presence of a tin oxide-rich overlayer, as pointed out by XPS. As a consequence of this, the electrocatalytic behavior of the catalysts was not influenced by the Ti/Sn ratio and was mainly dependent on the synthesis method used in the preparation of composite support materials. Elemental maps confirmed that in this type of electrocatalyst there were areas where Pt and the Sn doping element were in close proximity to each other, which ensured favorable surface sites both for the bifunctional mechanism and the electronic ligand effect.

A noticeable increase in both the ECSA values and the CO electrooxidation activity was observed on catalysts prepared using composite materials synthesized via route ***B***. An increase in carbon content in composite materials led to an increase of both catalytic activity and long-term stability. In addition, electrochemical stability tests showed that the best long-term stability result was obtained on the catalyst supported on composite with 75 wt% of carbon prepared with an extended aging period of 7 days. The results of electrochemical studies showed that Sn-containing Pt catalysts with a high carbon content (75 wt%) are the most promising for potential use both as an anode and a cathode for PEM fuel cells.

CRediT authorship contribution statement

András Tompos: Writing – review & editing, Supervision, Funding acquisition. **Stefan Neatu:** Investigation. **Dana Radu:** Investigation. **Andrei Kuncser:** Investigation. **Zoltán Pászti:** Writing – original draft, Validation, Methodology, Investigation, Conceptualization. **György Sáfrán:** Validation, Investigation. **Dániel Olasz:** Investigation. **István E. Sajó:** Investigation. **Emília Tálas:** Writing – review & editing, Methodology. **Khirdakhanim Salmanzade:** Investigation. **Mihaela Florea:** Writing – review & editing, Supervision. **Irina Borbáth:** Writing – original draft, Validation, Methodology, Investigation, Formal analysis, Conceptualization. **Ágnes Szegedi:** Investigation.

Declaration of Competing Interest

The authors declare that they have no known competing financial interests or personal relationships that could have appeared to influence the work reported in this paper.

Data Availability

Data will be made available on request.

Acknowledgement

This research was funded by Project no. RRF-2.3.1–21–2022–00009, titled National Laboratory for Renewable Energy has been implemented with the support provided by the Recovery and Resilience Facility of the European Union within the framework of Programme Széchenyi Plan Plus. Project No. NNE 131270 has been implemented with the support provided from the National Research, Development and Innovation Fund of Hungary financed under the M-ERA.NET-2018 funding scheme. AK, DR, SN and MF acknowledge: This work was supported by the Romanian National Authority for Scientific Research and Innovation, UEFISCDI, project number PN-III-P2–2.1-PTE-2021–0592 (Bio-energCell) and Ministry of Research, Innovation and Digitization through the Core Program 2023–2026 (contract PC3-PN23080303). Project no. C1792954 has been implemented with the support provided by the Ministry of Culture and Innovation of Hungary from the National Research, Development and Innovation Fund, financed under the KDP-2021 funding scheme. Support from Hungarian Scientific Research Fund OTKA, Grant number K143216 is also greatly acknowledged.

Appendix A. Supporting information

Supplementary data associated with this article can be found in the online version at doi:10.1016/j.cattod.2024.114788.

References

[1] B.G. Pollet, S.S. Kocha, I. Staffell, Current status of automotive fuel cells for sustainable transport, Curr. Opin. Electrochem. 16 (2019) 90–95, https://doi.org/10.1016/j.coelec.2019.04.021.
[2] J.C. Meier, C. Galeano, I. Katsounaros, A.A. Topalov, A. Kostka, F. Schu, K.J. J. Mayrhofer, Degradation mechanisms of Pt/C fuel cell catalysts under simulated start – stop conditions, ACS Catal. 2 (5) (2012) 832–843, https://doi.org/10.1021/cs300024h.
[3] J. Zhao, X. Li, A review of polymer electrolyte membrane fuel cell durability for vehicular applications: Degradation modes and experimental techniques, Energy Convers. Manag. 199 (2019) 112022, https://doi.org/10.1016/j.enconman.2019.112022.
[4] Ş. Neaţu, F. Neaţu, I.M. Chirica, I. Borbáth, E. Tálas, A. Tompos, S. Somacescu, P. Osiceanu, M.A. Folgado, A.M. Chaparro, M. Florea, Recent progress in electrocatalysts and electrodes for portable fuel cells, J. Mater. Chem. A 9 (2021) 17065–17128, https://doi.org/10.1039/d1ta03644k.

[5] S. Zhang, Y. Shao, G. Yin, Y. Lin, Recent progress in nanostructured electrocatalysts for PEM fuel cells, J. Mater. Chem. A. 1 (2013) 4631–4641, https://doi.org/10.1039/c3ta01161e.

[6] M.F. Mathias, R. Makharia, H.A. Gasteiger, J.J. Conley, T.J. Fuller, C. J. Gittleman, S.S. Kocha, D.P. Miller, C.K. Mittelsteadt, T. Xie, S.G. Yan, P.T. Yu, Two fuel cell cars in every garage? Electrochem. Soc. Interface 14 (2005) 24–35, https://doi.org/10.1149/2.f05053if.

[7] K.A. Kurdin, V.V. Kuznetsov, V.V. Sinitsyn, E.A. Galitskaya, E.A. Filatova, C. A. Belina, K.J. Stevenson, Synthesis and characterization of Pt-H_xMoO_3 catalysts for CO-tolerant PEMFCs, Catal. Today 388–389 (2022) 147–157, https://doi.org/10.1016/j.cattod.2020.07.079.

[8] E. Antolini, Catalysts for direct ethanol fuel cells, J. Power Sources 170 (2007) 1–12, https://doi.org/10.1016/j.jpowsour.2007.04.009.

[9] M. González-Hernández, E. Antolini, J. Perez, Synthesis, characterization and CO tolerance evaluation in PEMFCs of Pt_2RuMo electrocatalysts, Catalysts 9 (2019), https://doi.org/10.3390/catal9010061.

[10] L.G.S. Pereira, V.A. Paganin, E.A. Ticianelli, Investigation of the CO tolerance mechanism at several Pt-based bimetallic anode electrocatalysts in a PEM fuel cell, Electrochim. Acta 54 (2009) 1992–1998, https://doi.org/10.1016/j.electacta.2008.07.003.

[11] Z. Yan, J. Xie, J. Jing, M. Zhang, W. Wei, S. Yin, MoO_2 nanocrystals down to 5 nm as Pt electrocatalyst promoter for stable oxygen reduction reaction, Int. J. Hydrog. Energy 37 (2012) 15948–15955, https://doi.org/10.1016/j.ijhydene.2012.08.033.

[12] P.F.B.D. Martins, E.A. Ticianelli, Electrocatalytic activity and stability of platinum nanoparticles supported on carbon – molybdenum oxides for the oxygen reduction reaction, ChemElectroChem 2 (2015) 1298–1306, https://doi.org/10.1002/celc.201500196.

[13] C. Molochas, P. Tsiakaras, Carbon monoxide tolerant Pt-based electrocatalysts for H_2-PEMFC applications: current progress and challenges, Catalysts 11 (2021) 1127, https://doi.org/10.3390/catal11091127.

[14] D.W.G. Stewart, K. Scott, A.J. Wain, T.E. Rosser, E. Brightman, D. MacPhee, M. Mamlouk, The role of tungsten oxide in enhancing the carbon monoxide tolerance of platinum-based hydrogen oxidation catalysts, ACS Appl. Mater. Interfaces 12 (2020) 37079–37091, https://doi.org/10.1021/acsami.0c07804.

[15] K.J.J. Mayrhofer, K. Hartl, V. Juhart, M. Arenz, Degradation of carbon-supported Pt bimetallic nanoparticles by surface segregation, J. Am. Chem. Soc. 131 (2009) 16348–16349, https://doi.org/10.1021/ja9074216.

[16] A. Hassan, E.A. Ticianelli, Activity and stability of dispersed multi metallic Pt-based catalysts for CO Tolerance in proton exchange membrane fuel cell anodes, Acad. Bras. Cienc. 90 (2018) 697–718, https://doi.org/10.1590/0001-3765201820170559.

[17] P. He, T. Cheng, R. Bashyam, A.P. Young, S. Knights, Relative humidity effect on anode durability in PEMFC startup/shutdown processes, ECS Trans. 33 (2010) 1273–1279, https://doi.org/10.1149/1.3484620.

[18] S. Wang, C. Zhou, G. Shu, Y. Cao, L. Fan, L. Song, K. Ma, H. Yue, Insights into the effects of Pt and PtO_x site for electrocatalytic water gas shift reaction via altering supports and calcinated temperatures, Int. J. Hydrog. Energy 48 (2023) 24730–24741, https://doi.org/10.1016/j.ijhydene.2022.09.098.

[19] Q. Lv, M. Yin, X. Zhao, C. Li, C. Liu, W. Xing, Promotion effect of TiO_2 on catalytic activity and stability of Pt catalyst for electrooxidation of methanol, J. Power Sources 218 (2012) 93–99, https://doi.org/10.1016/j.jpowsour.2012.06.051.

[20] S.Y. Huang, P. Ganesan, S. Park, B.N. Popov, Development of a titanium dioxide-supported platinum catalyst with ultrahigh stability for polymer electrolyte membrane fuel cell applications, J. Am. Chem. Soc. 131 (2009) 13898–13899, https://doi.org/10.1021/ja904810h.

[21] R. Ganesan, J.S. Lee, An electrocatalyst for methanol oxidation based on tungsten trioxide microspheres and platinum, J. Power Sources 157 (2006) 217–221, https://doi.org/10.1016/j.jpowsour.2005.07.069.

[22] X. Cui, H. Zhang, X. Dong, H. Chen, L. Zhang, L. Shi, Electrochemical catalytic activity for the hydrogen oxidation of mesoporous WO_3 and WO_3/C composites, J. Mater. Chem. 30 (2008) 3575–3580, https://doi.org/10.1039/b806115g.

[23] F. Micoud, F. Maillard, A. Bonnefont, N. Job, M. Chatenet, The role of the support in CO_{ads} monolayer electrooxidation on Pt nanoparticles: Pt/WO_x vs. Pt/C, Phys. Chem. Chem. Phys. 12 (2010) 1182–1193, https://doi.org/10.1039/B915244J.

[24] J. Liu, L. Jiang, Electrostatic self-assembly of Pt nanoparticles on hexagonal tungsten oxide as an active CO-tolerant hydrogen oxidation electrocatalyst, Int. J. Hydrog. Energy 43 (2018) 8944–8952, https://doi.org/10.1016/j.ijhydene.2018.03.131.

[25] F. Micoud, F. Maillard, A. Gourgaud, M. Chatenet, Unique CO-tolerance of Pt-WO_x materials, Electrochem. Commun. 11 (2009) 651–654, https://doi.org/10.1016/j.elecom.2009.01.007.

[26] Y. Wang, E.R. Fachini, G. Cruz, Y. Zhu, Y. Ishikawa, J.A. Colucci, C.R. Cabrera, Effect of surface composition of electrochemically codeposited platinum/molybdenum oxide on methanol oxidation, J. Electrochem. Soc. 148 (2001) C222–C226, https://doi.org/10.1149/1.1349881.

[27] R. Li, H. Hao, T. Huang, A. Yu, Electrodeposited Pd-MoO_x catalysts with enhanced catalytic activity for formic acid electrooxidation, Electrochim. Acta 76 (2012) 292–299, https://doi.org/10.1016/j.electacta.2012.05.041.

[28] H. Zhang, C. Hu, X. He, L. Hong, G. Du, Y. Zhang, Pt support of multidimensional active sites and radial channels formed by SnO_2 flower-like crystals for methanol and ethanol oxidation, J. Power Sources 196 (2011) 4499–4505, https://doi.org/10.1016/j.jpowsour.2011.01.030.

[29] W.S. Baker, J.J. Pietron, M.E. Teliska, P.J. Bouwman, D.E. Ramaker, K.E. Swider-Lyons, Enhanced oxygen reduction activity in acid by tin-oxide supported Au nanoparticle catalysts, J. Electrochem. Soc. 153 (2006) A1702–A1707, https://doi.org/10.1149/1.2216527.

[30] E. Zhu, M. Wu, H. Xu, B. Peng, Z. Liu, Y. Huang, Y. Li, Stability of platinum-group-metal-based electrocatalysts in proton exchange membrane fuel cells, Adv. Funct. Mater. 32 (2022) 2203883, https://doi.org/10.1002/adfm.202203883.

[31] Y. Zhu, Q. Lin, Y. Zhong, H.A. Tahini, Z. Shao, H. Wang, Metal oxide-based materials as an emerging family of hydrogen evolution electrocatalysts, Energy Environ. Sci. 13 (2020) 3361–3392, https://doi.org/10.1039/d0ee02485f.

[32] T. Ioroi, Z. Siroma, S. Yamazaki, K. Yasuda, Electrocatalysts for PEM Fuel Cells, Adv. Energy Mater. 9 (2019) 1801284, https://doi.org/10.1002/aenm.201801284.

[33] Y. Takabatake, Z. Noda, S.M. Lyth, A. Hayashi, K. Sasaki, Cycle durability of metal oxide supports for PEFC electrocatalysts, Int. J. Hydrog. Energy 39 (2014) 5074–5082, https://doi.org/10.1016/j.ijhydene.2014.01.094.

[34] D. Wang, C.V. Subban, H. Wang, E. Rus, F.J. Disalvo, H.D. Abruña, Highly stable and CO-tolerant Pt/$Ti_{0.7}W_{0.3}O_2$ electrocatalyst for proton-exchange membrane fuel cells, J. Am. Chem. Soc. 132 (2010) 10218–10220, https://doi.org/10.1021/ja102931d.

[35] X. Cui, F. Cui, Q. He, L. Guo, M. Ruan, J. Shi, Graphitized mesoporous carbon supported Pt-SnO_2 nanoparticles as a catalyst for methanol oxidation, Fuel 89 (2010) 372–377, https://doi.org/10.1016/j.fuel.2009.09.006.

[36] L. Jiang, L. Colmenares, Z. Jusys, G.Q. Sun, R.J. Behm, Ethanol electrooxidation on novel carbon supported Pt/SnO_x/C catalysts with varied Pt:Sn ratio, Electrochim. Acta 53 (2007) 377–389, https://doi.org/10.1016/j.electacta.2007.01.047.

[37] A. Sandoval-Gonzalez, E. Borja-Arco, J. Escalante, O. Jimenez-Sandoval, S. A. Gamboa, Methanol oxidation reaction on $PtSnO_2$ obtained by microwave-assisted chemical reduction, Int. J. Hydrog. Energy 37 (2012) 1752–1759, https://doi.org/10.1016/j.ijhydene.2011.10.049.

[38] D.F. Silva, A.N. Geraldes, A.O. Neto, E.S. Pino, M. Linardi, E.V. Spinacé, W.A. A. Macedo, J.D. Ardisson, Preparation of $PtSnO_2$/C electrocatalysts using electron beam irradiation, Mater. Sci. Eng. 175 (2010) 261–265, https://doi.org/10.1016/j.mseb.2010.08.002.

[39] L. Jiang, G. Sun, Z. Zhou, S. Sun, Q. Wang, S. Yan, H. Li, J. Tian, J. Guo, B. Zhou, Q. Xin, Size-controllable synthesis of monodispersed SnO_2 nanoparticles and application in electrocatalysts, J. Phys. Chem. B. 109 (2005) 8774–8778, https://doi.org/10.1021/jp050334g.

[40] E. Higuchi, K. Miyata, T. Takase, H. Inoue, Ethanol oxidation reaction activity of highly dispersed Pt/SnO_2 double nanoparticles on carbon black, J. Power Sources 196 (2011) 1730–1737, https://doi.org/10.1016/j.jpowsour.2010.10.008.

[41] A. Bach Delpeuch, F. Maillard, M. Chatenet, P. Soudant, C. Cremers, Ethanol oxidation reaction (EOR) investigation on Pt/C, Rh/C, and Pt-based bi- and tri-metallic electrocatalysts: A DEMS and in situ FTIR study, Appl. Catal. B Environ. 181 (2016) 672–680, https://doi.org/10.1016/j.apcatb.2015.08.041.

[42] K. Ke, K. Waki, Fabrication and characterization of multiwalled carbon nanotubes-supported Pt/SnO_x nanocomposites as catalysts for electro-oxidation of methanol, J. Electrochem. Soc. 154 (2007) A207–A212, https://doi.org/10.1149/1.2426873.

[43] M. Li, W.P. Zhou, N.S. Marinkovic, K. Sasaki, R.R. Adzic, The role of rhodium and tin oxide in the platinum-based electrocatalysts for ethanol oxidation to CO_2, Electrochim. Acta 104 (2013) 454–461, https://doi.org/10.1016/j.electacta.2012.10.046.

[44] S. von Kraemer, K. Wikander, G. Lindbergh, A. Lundblad, A.E.C. Palmqvist, Evaluation of TiO_2 as catalyst support in Pt-TiO_2/C composite cathodes for the proton exchange membrane fuel cell, J. Power Sources 180 (2008) 185–190, https://doi.org/10.1016/j.jpowsour.2008.02.023.

[45] W. Vogel, L. Timperman, N. Alonso-Vante, Probing metal substrate interaction of Pt nanoparticles: Structural XRD analysis and oxygen reduction reaction, Appl. Catal. A Gen. 377 (2010) 167–173, https://doi.org/10.1016/j.apcata.2010.01.034.

[46] B. Abida, L. Chirchi, S. Baranton, T.W. Napporn, H. Kochkar, J.M. Léger, A. Ghorbel, Preparation and characterization of Pt/TiO_2 nanotubes catalyst for methanol electro-oxidation, Appl. Catal. B Environ. 106 (2011) 609–615, https://doi.org/10.1016/j.apcatb.2011.06.022.

[47] X.L. Sui, Z.B. Wang, M. Yang, L. Huo, D.M. Gu, G.P. Yin, Investigation on C-TiO_2 nanotubes composite as Pt catalyst support for methanol electrooxidation, J. Power Sources 255 (2014) 43–51, https://doi.org/10.1016/j.jpowsour.2014.01.001.

[48] R. Kou, Y. Shao, D. Mei, Z. Nie, D. Wang, C. Wang, V.V. Viswanathan, S. Park, I. A. Aksay, Y. Lin, Y. Wang, J. Liu, Stabilization of electrocatalytic metal nanoparticles at metal-metal oxide-graphene triple junction points, J. Am. Chem. Soc. 133 (2011) 2541–2547, https://doi.org/10.1021/ja107719u.

[49] C. Marichy, G. Ercolano, G. Caputo, M.G. Willinger, D. Jones, J. Rozière, N. Pinna, S. Cavaliere, ALD SnO_2 protective decoration enhances the durability of a Pt based electrocatalyst, J. Mater. Chem. A. 4 (2016) 969, https://doi.org/10.1039/C5TA08432F.

[50] E. Antolini, E.R. Gonzalez, Ceramic materials as supports for low-temperature fuel cell catalysts, Solid State Ion. 180 (2009) 746–763, https://doi.org/10.1016/j.ssi.2009.03.007.

[51] M.S. Saha, R. Li, X. Sun, Composite of Pt-Ru supported SnO_2 nanowires grown on carbon paper for electrocatalytic oxidation of methanol, Electrochem. Commun. 9 (2007) 2229–2234, https://doi.org/10.1016/j.elecom.2007.06.032.

[52] S. Sago, A.B. Suryamas, G.M. Anilkumar, T. Ogi, K. Okuyama, In situ growth of Pt nanoparticles on electrospun SnO_2 fibers for anode electrocatalyst application, Mater. Lett. 105 (2013) 202–205, https://doi.org/10.1016/j.matlet.2013.04.007.

[53] A.B. Suryamas, G.M. Anilkumar, S. Sago, T. Ogi, K. Okuyama, Electrospun Pt/SnO_2 nanofibers as an excellent electrocatalysts for hydrogen oxidation reaction with ORR-blocking characteristic, Catal. Commun. 33 (2013) 11–14, https://doi.org/10.1016/j.catcom.2012.12.014.

[54] C.V. Subban, Q. Zhou, A. Hu, T.E. Moylan, F.T. Wagner, F.J. Disalvo, Sol-gel synthesis, electrochemical characterization, and stability testing of $Ti_{0.7}W_{0.3}O_2$ nanoparticles for catalyst support applications in proton-exchange membrane fuel cells, J. Am. Chem. Soc. 132 (2010) 17531–17536, https://doi.org/10.1021/ja1074163.

[55] V.T.T. Ho, C.J. Pan, J. Rick, W.N. Su, B.J. Hwang, Nanostructured $Ti_{0.7}Mo_{0.3}O_2$ support enhances electron transfer to Pt: High-performance catalyst for oxygen reduction reaction, J. Am. Chem. Soc. 133 (2011) 11716–11724, https://doi.org/10.1021/ja2039562.

[56] T.T. Nguyen, V.T.T. Ho, C.J. Pan, J.Y. Liu, H.L. Chou, J. Rick, W.N. Su, B. J. Hwang, Synthesis of $Ti_{0.7}Mo_{0.3}O_2$ supported-Pt nanodendrites and their catalytic activity and stability for oxygen reduction reaction, Appl. Catal. B Environ. 154–155 (2014) 183–189, https://doi.org/10.1016/j.apcatb.2014.02.018.

[57] K.W. Park, K.S. Seol, Nb-TiO_2 supported Pt cathode catalyst for polymer electrolyte membrane fuel cells, Electrochem. Commun. 9 (2007) 2256–2260, https://doi.org/10.1016/j.elecom.2007.06.027.

[58] S.Y. Huang, P. Ganesan, B.N. Popov, Electrocatalytic activity and stability of niobium-doped titanium oxide supported platinum catalyst for polymer electrolyte membrane fuel cells, Appl. Catal. B Environ. 96 (2010) 224–231, https://doi.org/10.1016/j.apcatb.2010.02.025.

[59] A. Kumar, V. Ramani, $Ta_{0.3}Ti_{0.7}O_2$ Electrocatalyst Supports Exhibit Exceptional Electrochemical Stability, J. Electrochem. Soc. 160 (2013) F1207–F1215, https://doi.org/10.1149/2.038311jes.

[60] X. Liu, X. Wu, K. Scott, Study of niobium and tantalum doped titania supported Pt electrocatalysts for methanol oxidation and oxygen reduction reactions, Catal. Sci. Technol. 4 (2014) 3891–3898, https://doi.org/10.1039/C4CY00393D.

[61] Y. Gao, M. Hou, Z. Shao, C. Zhang, X. Qin, B. Yi, Preparation and characterization of $Ti_{0.7}Sn_{0.3}O_2$ as catalyst support for oxygen reduction reaction, J. Energy Chem. 23 (2014) 331–337, https://doi.org/10.1016/S2095-4956(14)60155-8.

[62] K. Zakrzewska, M. Radecka, M. Rekas, Effect of Nb, Cr, Sn additions on gas sensing properties of TiO_2 thin films, Thin Solid Films 310 (1997) 161–166, https://doi.org/10.1016/S0040-6090(97)00401-X.

[63] A. Sengele, D. Robert, N. Keller, C. Colbeau-Justin, V. Keller, Sn-doped and porogen-modified TiO_2 photocatalyst for solar light elimination of sulfure diethyle as a model for chemical warfare agent, Appl. Catal. B Environ. 245 (2019) 279–289, https://doi.org/10.1016/j.apcatb.2018.12.071.

[64] I. Rangel-Vázquez, G. Del Angel, V. Bertin, F. González, A. Vázquez-Zavala, A. Arrieta, J.M. Padilla, A. Barrera, E. Ramos-Ramirez, Synthesis and characterization of Sn doped TiO_2 photocatalysts: Effect of Sn concentration on the textural properties and on the photocatalytic degradation of 2,4-dichloro-phenoxyacetic acid, J. Alloy. Compd. 643 (2015) S144–S149, https://doi.org/10.1016/j.jallcom.2014.12.065.

[65] M.M. Oliveira, D.C. Schnitzler, A.J.G. Zarbin, (Ti,Sn)O_2 mixed oxides nanoparticles obtained by the Sol−Gel route, Chem. Mater. 15 (2003) 1903–1909, https://doi.org/10.1021/cm0210344.

[66] S. Mahanty, S. Roy, S. Sen, Effect of Sn doping on the structural and optical properties of sol-gel TiO_2 thin films, J. Cryst. Growth 261 (2004) 77–81, https://doi.org/10.1016/j.jcrysgro.2003.09.023.

[67] M. Afuyoni, G. Nashed, I.M. Nasser, TiO_2 doped with SnO_2 and studing its structurail and electrical properties, Energy Procedia 6 (2011) 11–20, https://doi.org/10.1016/j.egypro.2011.05.002.

[68] S.K. Kulshreshtha, R. Sasikala, V. Sudarsan, Non-random distribution of cations in $Sn_{1-x}Ti_xO_2$ ($0.0 \leq x \leq 1.0$): a ^{119}Sn MAS NMR study, J. Mater. Chem. 11 (2001) 930–935, https://doi.org/10.1039/b006258h.

[69] B. Sun, T. Shi, Z. Peng, W. Sheng, T. Jiang, G. Liao, Controlled fabrication of Sn/TiO_2 nanorods for photoelectrochemical water splitting, Nanoscale Res. Lett. 8 (2013) 462, https://doi.org/10.1186/1556-276X-8-462.

[70] L.B. Kong, J. Ma, H. Huang, Preparation of the solid solution $Sn_{0.5}Ti_{0.5}O_2$ from an oxide mixture via a mechanochemical process, J. Alloy. Compd. 336 (2002) 315–319, https://doi.org/10.1016/S0925-8388(01)01894-1.

[71] P.R. Bueno, M.R. Cassia-santos, L.G.P. Simões, W. Gomes, E. Longo, A. Varela, Low-Voltage Varistor Based on (Sn,Ti)O_2 Ceramics, J. Am. Ceram. Soc. 85 (2002) 282–284, https://doi.org/10.1111/j.1151-2916.2002.tb00084.x.

[72] J. Lin, J.C. Yu, D. Lo, S.K. Lam, Photocatalytic activity of rutile $Ti_{1-x}Sn_xO_2$ solid solutions, J. Catal. 183 (1999) 368–372, https://doi.org/10.1006/jcat.1999.2409.

[73] Y. Cao, W. Yang, W. Zhang, G. Liu, P. Yue, Improved photocatalytic activity of Sn^{4+} doped TiO_2 nanoparticulate films prepared by plasma-enhanced chemical vapor deposition, New. J. Chem. 28 (2004) 218–222, https://doi.org/10.1039/B306845E.

[74] Y.F. Tu, S.Y. Huang, J.P. Sang, X.W. Zou, Synthesis and photocatalytic properties of Sn-doped TiO_2 nanotube arrays, J. Alloy. Compd. 482 (2009) 382–387, https://doi.org/10.1016/j.jallcom.2009.04.027.

[75] J. Yu, S. Liu, M. Zhou, Enhanced photocalytic activity of hollow anatase microspheres by Sn^{4+} incorporation, J. Phys. Chem. C. 112 (2008) 2050–2057, https://doi.org/10.1021/jp0770007.

[76] K.N.P. Kumar, D.J. Fray, J. Nair, F. Mizukami, T. Okubo, Enhanced anatase-to-rutile phase transformation without exaggerated particle growth in nanostructured titania-tin oxide composites, Scr. Mater. 57 (2007) 771–774, https://doi.org/10.1016/j.scriptamat.2007.06.039.

[77] Y. Cao, T. He, L. Zhao, E. Wang, W. Yang, Y. Cao, Structure and phase transition behavior of Sn^{4+}-doped TiO_2 nanoparticles, J. Phys. Chem. C. 113 (2009) 18121–18124, https://doi.org/10.1021/jp9069288.

[78] Y. Li, C. Liu, Y. Liu, B. Feng, L. Li, H. Pan, W. Kellogg, D. Higgins, G. Wu, Sn-doped TiO_2 modified carbon to support Pt anode catalysts for direct methanol fuel cells, J. Power Sources 286 (2015) 354–361, https://doi.org/10.1016/j.jpowsour.2015.03.155.

[79] D. Gubán, I. Borbáth, Z. Pászti, I. Sajó, E. Drotár, M. Hegedűs, A. Tompos, Preparation and characterization of novel $Ti_{0.7}W_{0.3}O_2$-C composite materials for Pt-based anode electrocatalysts with enhanced CO tolerance, Appl. Catal. B Environ. 174–175 (2015) 455–470, https://doi.org/10.1016/j.apcatb.2015.03.031.

[80] Á. Vass, I. Borbáth, Z. Pászti, I. Bakos, I.E. Sajó, P. Németh, A. Tompos, Effect of Mo incorporation on the electrocatalytic performance of Ti–Mo mixed oxide–carbon composite supported Pt electrocatalysts, React. Kinet. Mech. Catal. 121 (2017) 141–160, https://doi.org/10.1007/s11144-017-1155-5.

[81] I. Borbáth, K. Zelenka, Á. Vass, Z. Pászti, G.P. Szijjártó, Z. Sebestyén, G. Sáfrán, A. Tompos, CO tolerant Pt electrocatalysts for PEM fuel cells with enhanced stability against electrocorrosion, Int. J. Hydrog. Energy 46 (2021) 13534–13547, https://doi.org/10.1016/j.ijhydene.2020.08.002.

[82] I. Borbáth, E. Tálas, Z. Pászti, K. Zelenka, I. Ayyubov, K. Salmanzade, I.E. Sajó, G. Sáfrán, A. Tompos, Investigation of Ti-Mo mixed oxide-carbon composite supported Pt electrocatalysts: Effect of the type of carbonaceous materials, Appl. Catal. A Gen. 620 (2021) 118155, https://doi.org/10.1016/j.apcata.2021.118155.

[83] M.S. Yazici, S. Dursun, I. Borbáth, A. Tompos, Reformate gas composition and pressure effect on CO tolerant Pt/$Ti_{0.8}Mo_{0.2}O_2$–C electrocatalyst for PEM fuel cells, Int. J. Hydrog. Energy 46 (2021) 13524–13533, https://doi.org/10.1016/j.ijhydene.2020.08.226.

[84] D. Gubán, A. Tompos, I. Bakos, Vass, Z. Pászti, E.G. Szabó, I.E. Sajó, I. Borbáth, Preparation of CO-tolerant anode electrocatalysts for polymer electrolyte membrane fuel cells, Int. J. Hydrog. Energy 42 (2017) 13741–13753, https://doi.org/10.1016/j.ijhydene.2017.03.080.

[85] F.E. Oropeza, B. Davies, R.G. Palgrave, R.G. Egdell, Electronic basis of visible region activity in high area Sn-doped rutile TiO_2 photocatalysts, Phys. Chem. Chem. Phys. 13 (2011) 7882–7891, https://doi.org/10.1039/c0cp02639e.

[86] G.S. Pawley, Unit-cell refinement from powder diffraction scans, J. Appl. Cryst. 14 (1981) 357–361, https://doi.org/10.1107/S0021889881009618.

[87] W.S. Rasband, ImageJ, (n.d.). ⟨https://imagej.net/ij/⟩.

[88] N. Fairley, CasaXPS: Spectrum Processing Software for XPS, AES and SIMS (Version 2.3.13), Cheshire. (2006). ⟨http://www.casaxps.com/⟩.

[89] M. Mohai, XPS MultiQuant: Multimodel XPS quantification software, Surf. Interface Anal. 36 (2004) 828–832, https://doi.org/10.1002/sia.1775.

[90] M. Mohai, XPS MultiQuant: Multi-model X-ray photoelectron spectroscopy quantification program, (Version 7.00.92), (2011).http://aki.ttk.mta.hu/XMQpages/XMQhome.php.

[91] C.D. Wagner, A.V. Naumkin, A. Kraut-Vass, S.W. Gaarenstroom, J.C. Powell, W. Allison, C.J. Powell, J.R.J. Rumble, NIST X-ray Photoelectron Spectroscopy Database, (2003). https://srdata.nist.gov/xps/ (accessed June 2, 2021).

[92] J.F. Moulder, W.F. Stickle, P.E. Sobol, K.D. Bombe, Handbook of X-ray Photoelectron Spectroscopy, Perkin-Elmer Corp. Eden Prairie, Minnesota, USA, 1992.

[93] R. Woods, in: M. Dekker (Ed.), Electroanalytical Chemistry: A Series of Advances, Basel, New York, 1976.

[94] I. Ayyubov, E. Tálas, K. Salmanzade, A. Kuncser, Z. Pászti, Ş. Neaţu, A.G. Mirea, M. Florea, A. Tompos, I. Borbáth, Electrocatalytic properties of mixed-oxide-containing composite-supported platinum for polymer electrolyte membrane (PEM) fuel cells, Mater. (Basel) 15 (2022) 3671, https://doi.org/10.3390/ma15103671.

[95] A.R. Mitchell, R.H. Parker, The reduction of SnO_2 and Fe_2O_3 by solid carbon, Miner. Eng. 1 (1988) 53–66, https://doi.org/10.1016/0892-6875(88)90066-0.

[96] S.P.S. Porto, P.A. Fleury, T.C. Damen, Raman spectra of TiO_2, MgF_2, ZnF_2, FeF_2, and MnF_2, Phys. Rev. 154 (1967) 522–526, https://doi.org/10.1103/PhysRev.154.522.

[97] M. Gotić, M. Ivanda, S. Popović, S. Musić, A. Sekulić, A. Turkovic, K. Furić, Raman investigation of nanosized TiO_2, J. Raman Spectrosc. 28 (1997) 555–558, https://doi.org/10.1002/(sici)1097-4555(199707)28:7<555::aid-jrs118>3.3.co;2-j.

[98] F. Tuinstra, J.L. Koenig, Raman Spectrum of Graphite, J. Chem. Phys. 53 (1970) 1126–1130, https://doi.org/10.1063/1.1674108.

[99] Z. Zhang, J. Liu, J. Gu, L. Su, L. Cheng, An overview of metal oxide materials as electrocatalysts and supports for polymer electrolyte fuel cells, Energy Environ. Sci. 7 (2014) 2535–2558, https://doi.org/10.1039/c3ee43886d.

[100] D. Pantea, H. Darmstadt, S. Kaliaguine, C. Roy, Electrical conductivity of conductive carbon blacks: Influence of surface chemistry and topology, Appl. Surf. Sci. 217 (2003) 181–193, https://doi.org/10.1016/S0169-4332(03)00550-6.

[101] D. Dicházi, I. Borbáth, I. Bakos, G.P. Szijjártó, A. Tompos, Z. Pászti, Design of Mo-doped mixed oxide–carbon composite supports for Pt-based electrocatalysts: the nature of the Mo-Pt interaction, Catal. Today 366 (2021) 31–40, https://doi.org/10.1016/j.cattod.2020.04.004.

[102] C. Silva, K. Salmanzade, I. Borbáth, E. Dódony, D. Olasz, G. Sáfrán, A. Kuncser, E. Pászti-Gere, A. Tompos, Z. Pászti, Reductive treatment of Pt supported on $Ti_{0.8}Sn_{0.2}O_2$-C composite: a route for modulating the Sn–Pt interactions, Nanomaterials 13 (2023) 2245, https://doi.org/10.3390/nano13152245.

[103] I. Borbáth, D. Gubán, I. Bakos, Z. Pászti, G. Gajdos, I.E. Sajó, Vass, A. Tompos, Exclusive formation of alloy phases via anchoring technique—From bimetallic catalysts to electrocatalysis, Catal. Today 306 (2018) 58–70, https://doi.org/10.1016/j.cattod.2017.01.011.

[104] F. Maillard, S. Schreier, M. Hanzlik, E.R. Savinova, S. Weinkauf, U. Stimming, Influence of particle agglomeration on the catalytic activity of carbon-supported Pt nanoparticles in CO monolayer oxidation, Phys. Chem. Chem. Phys. 7 (2005) 375–383, https://doi.org/10.1039/b411377b.

[105] A. Bauer, C. Song, A. Ignaszak, R. Hui, J. Zhang, L. Chevallier, D. Jones, J. Rozière, Improved stability of mesoporous carbon fuel cell catalyst support through incorporation of TiO_2, Electro. Acta 55 (2010) 8365–8370, https://doi.org/10.1016/j.electacta.2010.07.025.

[106] X. Liu, J. Chen, G. Liu, L. Zhang, H. Zhang, B. Yi, Enhanced long-term durability of proton exchange membrane fuel cell cathode by employing Pt/TiO_2/C catalysts, J. Power Sources 195 (2010) 4098–4103, https://doi.org/10.1016/j.jpowsour.2010.01.077.

[107] T.N. Geppert, M. Bosund, M. Putkonen, B.M. Stühmeier, A.T. Pasanen, P. Heikkilä, H.A. Gasteiger, H.A. El-Sayed, HOR Activity of Pt-TiO_{2-Y} at Unconventionally High Potentials Explained: The Influence of SMSI on the Electrochemical Behavior of Pt, J. Electrochem. Soc. 167 (2020) 084517, https://doi.org/10.1149/1945-7111/ab90ae.

[108] M. Eckardt, C. Gebauer, Z. Jusys, M. Wassner, N. Hüsing, R.J. Behm, Oxygen reduction reaction activity and long-term stability of platinum nanoparticles supported on titania and titania-carbon nanotube composites, J. Power Sources 400 (2018) 580–591, https://doi.org/10.1016/j.jpowsour.2018.08.036.

[109] N. Dimakis, H. Iddir, R.R. Díaz-Morales, R. Lia, G. Bunker, E.-H. Chung, E. S. Smotkin, A band dispersion mechanism for Pt alloy compositional tuning of linear bound CO stretching frequencies, J. Phys. Chem. B. 109 (2005) 1839–1848, https://doi.org/10.1021/jp046332y.